



UNDERSTANDING THE INFLUENCE OF
TURBULENCE IN IMAGING
FOURIER-TRANSFORM SPECTROMETRY
OF SMOKESTACK PLUMES

THESIS

Jennifer L. Massman, Lieutenant, USAF
AFIT/GAP/ENP/11-M05

DEPARTMENT OF THE AIR FORCE
AIR UNIVERSITY

AIR FORCE INSTITUTE OF TECHNOLOGY

Wright-Patterson Air Force Base, Ohio

APPROVED FOR PUBLIC RELEASE; DISTRIBUTION UNLIMITED.

The views expressed in this thesis are those of the author and do not reflect the official policy or position of the United States Air Force, the Department of Defense, or the United States Government. This material is declared a work of the U.S. Government and is not subject to copyright protection in the United States.

AFIT/GAP/ENP/11-M05

UNDERSTANDING THE INFLUENCE OF TURBULENCE IN IMAGING
FOURIER-TRANSFORM SPECTROMETRY OF SMOKESTACK PLUMES

THESIS

Presented to the Faculty
Department of Engineering Physics
Graduate School of Engineering and Management
Air Force Institute of Technology
Air University
Air Education and Training Command
in Partial Fulfillment of the Requirements for the
Degree of Master of Science in Applied Physics

Jennifer L. Massman, BSME
Lieutenant, USAF


March 2011

APPROVED FOR PUBLIC RELEASE; DISTRIBUTION UNLIMITED.

UNDERSTANDING THE INFLUENCE OF TURBULENCE IN IMAGING
FOURIER-TRANSFORM SPECTROMETRY OF SMOKESTACK PLUMES

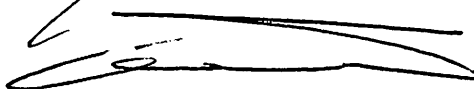
Jennifer L. Massman, BSME
Lieutenant, USAF

Approved:



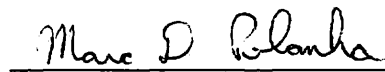
Kevin C. Gross, PhD (Chairman)

4-Mar-2011
Date



Glen P. Perram, PhD (Member)

4 MAR 2011
Date



Marc D. Polanka, PhD (Member)

4-mar-2011
Date

Abstract

An imaging Fourier-transform spectrometer (IFTS) was used to collect infrared hyper-spectral imagery of smokestack plume associated with coal-burning power facility to assess the influence of turbulence on spectral retrieval of temperature (T) and pollutant concentrations (C_i). A mid-wave (1.5-5.5 μm) Telops Hyper-Cam was used and features a 320x256 InSb focal-plane array with a 326 μrad instantaneous field-of-view (IFOV). The line-of-sight distance to the 76 m tall smokestack exit was 350 m (11.4 x 11.4 cm^2 IFOV). Approximately 5000 interferogram cubes were collected in 30 minutes on a 128x128 pixel window corresponding to a spectral resolution of 20 cm^{-1} . Radiance fluctuations due to plume turbulence were observed on a time scale much shorter than hyper-spectral image acquisition rate, thereby introducing scene change artifacts (SCA) in the Fourier-transformed spectra. Time-averaging the spectra minimizes SCA magnitudes, but accurate T and C_i retrieval would require a priori knowledge of the statistical distribution of temperature and other stochastic flow field parameters. A method of quantile sorting in interferogram space prior to Fourier-transformation is presented and used to identify turbulence throughout the plume. It is demonstrated that if radiance fluctuations are due only to temperature fluctuations, the spectrum associated with each interferogram quantile directly corresponds to the corresponding quantile temperature. Analysis of the quantile spectra indicate that radiance fluctuations are driven by more than just temperature fluctuations. Immediately above the stack exit, T and CO_2 concentration estimates from the median spectrum are 395 K and 6%, respectively, which compare well to *in situ* measurements. Turbulence is small above the stack exit and introduced systematic errors in T and C_i on the order of 0.5 K and 0.01%, respectively. In some plume locations,

turbulent fluctuations introduced errors in T and C_i on the order of 8 K and 1%, respectively. While more complicated radiance fluctuations precluded straightforward retrieval of the temperature probability distribution, the results demonstrate the utility of additional information content associated with multiple interferogram quantiles and suggest IFTS may find use as a tool for non-intrusive flow field analysis.

Acknowledgements

I owe my sincerest gratitude to my advisor, Dr. Kevin Gross, for his patient guidance throughout this process. His enthusiasm about the research was inspirational, and his consistent availability and willingness to help were instrumental. The many office hours spent helping me understand the concepts and guiding my next steps were invaluable to my learning and ability to accomplish what seemed like such an enormous task.

I would also like to express my gratitude to my family for all their love and support, especially my husband for his encouragement, patience, and for always being there for me.

Jennifer L. Massman

Table of Contents

	Page
Abstract	iv
Acknowledgements	vi
List of Figures	viii
I. Introduction	1
II. Background	5
2.1 Previous Work	5
2.1.1 Fourier Transform Infrared Spectrometry of Plumes.....	5
2.1.2 Imaging Fourier Transform Spectrometry of Turbulent Plumes	7
2.2 Theory.....	9
2.2.1 Fourier Transform Spectrometry	10
2.2.2 Spectral Modeling	12
2.2.3 Statistics Background	15
III. Understanding the Influence of Turbulence in Imaging Fourier Transform Spectrometry of Smokestack Plumes	17
3.1 Abstract	17
3.2 Introduction	18
3.3 Methodology.....	21
3.3.1 IFTS	21
3.3.2 Spectral Model.....	22
3.3.3 Turbulent Sources	25
3.3.4 Quantile Analysis Method	26
3.4 Experimental	29
3.4.1 Stack Measurements	29
3.4.2 Instrumentation	31
3.5 Results and Discussion	32
3.5.1 Spectral Imagery	33
3.5.2 Fit Results	35
3.5.3 Turbulence Simulations	44
3.6 Conclusions and Recommendations	48
Appendix A. Matlab Code	50
Bibliography	52

List of Figures

Figure		Page
1.	Images of a coal-burning smokestack plume changing with time.	2
2.	Diagram of a traditional Michelson interferometer.	10
3.	Cumulative distribution function and probability distribution function for the standard normal distribution.	15
4.	Images of a coal-burning smokestack plume changing with time.	19
5.	Difference in the model radiance at two temperatures: $L(\tilde{\nu}, 400K) - L(\tilde{\nu}, 390K)$	27
6.	Diagram of the coal-burning power plant and test observation point.	31
7.	Mean $L(\tilde{\nu})$ at 2238 cm^{-1} and mean spectra at several pixels. Mean $L(\tilde{\nu})$ - median $L(\tilde{\nu})$ at 2238 cm^{-1} and mean - mean spectra at several pixels.	35
8.	Mean and median spectral data and fit results with residuals for several pixels.	36
9.	Root mean squared error of $L_{mean}(\tilde{\nu})$ and spectral model (R_{mean}) and $R_{mean} - R_{med}$	38
10.	Mean, mean - median, standard deviation, and the difference between two standard deviation estimates of the brightness temperature, temperature, CO_2 concentration, and soot transmittance.	40
11.	Temperature, CO_2 concentration, and soot transmittance as a function of quantile for several pixels.	43
12.	Error due to temperature and concentration fluctuations in a turbulent plume.	45

UNDERSTANDING THE INFLUENCE OF TURBULENCE IN IMAGING FOURIER-TRANSFORM SPECTROMETRY OF SMOKESTACK PLUMES

I. Introduction

Fourier-transform spectrometry (FTS) has long been employed for the remote characterization of the spectra of chemical plumes. The ability to determine with confidence the species concentrations emitted from a smokestack without the need for *in situ* measurements has important intelligence and governmental applications. FTS presents the opportunity to remotely monitor smokestacks to verify adherence with environmental regulations without disruption of plant operations. The ability to simultaneously determine the concentrations of multiple chemical species make FTS an attractive option for the purpose of monitoring smokestack emissions. Its mobility, distance from the source, and the fact that FTS is a passive technique all provide the potential to monitor smokestacks undetected, making FTS advantageous for monitoring smokestack effluents for intelligence purposes as well. While previous research has demonstrated the capability of using non-imaging FTS to characterize plumes [1]-[6], the degree to which turbulence in smokestack plumes affects spectral interpretation is unknown. The accuracy of effluent concentrations obtained by non-imaging FTS can be improved upon by imaging Fourier-transform spectrometry (IFTS), which provides the additional spatial advantage over non-imaging FTS. Non-imaging FTS lacks the ability to isolate specific regions of the source, and the results can be affected by incorporating both turbulent and steady regions of the source or regions other than the source itself. IFTS possesses the ability to isolate specific regions of the plume and improve the accuracy of effluent concentration estimates. Because IFTS retains

the DC component of intensity, which is removed in virtually all non-imaging FTS, the spectra can be statistically sorted into quantile spectra. These quantile spectra provide additional information related to flow field fluctuations.

While IFTS is an efficient means for the remote characterization of a static source, problems arise when observing a turbulent source such as a smokestack plume. Turbulence due to temperature or concentration fluctuations in the plume introduces scene change artifacts (SCAs) which corrupt the spectra. Figure 1 shows images (0.1 seconds apart) captured with the Telops Hyper-Cam imaging spectrometer and shows the structure of the plume changing with time. These images demonstrate the presence of turbulent fluctuations in the plume, which must be taken into account to gain better confidence in effluent concentration estimates obtained by IFTS.

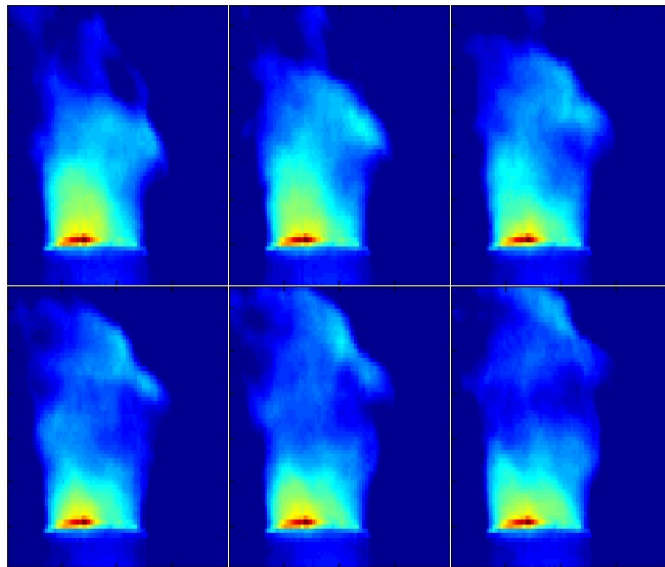


Figure 1. Images of a coal-burning smokestack plume changing with time captured with the Telops Hyper-Cam imaging spectrometer. The presence of turbulent fluctuations is apparent in the changing structure of the plume.

Because the radiative transfer model used to determine temperatures and effluent concentrations assumes a single temperature source, accurate interpretation of the

spectra requires an understanding of the underlying temperature distribution. Non-linearities in the spectral model result in a bias of temperatures (and hence concentrations) retrieved from the time-averaged spectrum. Thus knowledge of the underlying temperature distribution is required to accurately simulate the time-averaged spectrum. If both temperature and effluent concentrations are fluctuating, then knowledge of both the temperature and concentration distributions is necessary.

This research uses hyper-spectral imagery of a coal-burning smokestack plume obtained from the Telops Hyper-Cam imaging spectrometer to quantify the effects of turbulence on the proper interpretation of smokestack emissions for accurate pollutant concentration retrieval. In past studies, it has been shown that IFTS can be used to determine the effluents and concentrations of a turbulent source by reducing spectral artifacts through temporal averaging [7]-[9]. However, due to non-linearities in the model, use of the mean spectrum gives a biased estimate of temperature (and therefore concentrations). This research seeks to use a single-layer radiative transfer model to estimate temperature and column densities for each plume pixel. A novel method of processing the interferograms is employed that reduces spectral artifacts and under the correct conditions provides unbiased temperature and column density estimates. This method provides a means of understanding the effect of turbulence throughout the plume by leveraging the DC level imagery to produce quantile interferograms. Assuming only temperature is causing turbulent radiance fluctuations, quantile spectra can be mapped to corresponding quantile temperatures and the underlying temperature distribution discerned. This research seeks to use these quantile spectra to quantify the turbulence-driven radiance fluctuations and determine if temperature fluctuations are in fact the primary cause. This also enables the estimation of retrieved concentration confidence bounds which include the effects of turbulence. The potential of IFTS for general non-intrusive analysis of emissive flow fields is also

demonstrated. IFTS, because it retains the DC component of intensity, provides quantile spectra which contain fluctuation information across the plume. A simulation tool for modeling mid-wave infrared spectra of turbulent gas-phase sources is also developed.

Chapter 2 summarizes previous research relating to the remote observation of chemical plumes and the use of IFTS to observe turbulent sources. It also provides the necessary theoretical background for an understanding of the method of interferogram processing and spectral modeling used. Chapter 3 contains a conference paper detailing the methodology, experimental setup, results, and conclusions of this research.

II. Background

2.1 Previous Work

Non-imaging Fourier transform spectrometry has been widely used in the past to characterize the spectra of smokestack plumes. While research has shown effluent concentrations obtained from FTS to be consistent with *in situ* measurements, the accuracy of these measurements is limited by the instrument's ability to take in a uniform section of the plume. Imaging FTS presents the possibility of improving upon FTS measurements through its ability to isolate sections of the plume. Research has shown SCAs in the spectra that would discourage the use of IFTS to study turbulent sources can be reduced through temporal averaging [7]-[9] or a method of statistically sorting the interferograms [10].

2.1.1 Fourier-Transform Infrared Spectrometry of Plumes.

The use of FTS for the purpose of remotely monitoring smokestack emissions has been well researched in the past, often with the goal of a more efficient means of verifying emissions compliance, fence line monitoring, and other environmental monitoring problems. One application of FTS is the remote determination of the substances burned at a power plant. Carlson *et al.* used an FTS to study the emission spectra of the constituents of exhaust plumes from the smokestacks of small buildings. The main objective of this research was to establish the best process for determining whether gas or oil was being burned in the furnace. First, the chemical compositions and $\text{H}_2\text{O}/\text{CO}_2$ concentration ratios for oil and gas were calculated. Since the background was strong and fluctuated greatly relative to the weak emission characteristics of the effluents, it was necessary to utilize a method of spectral pattern recognition to diminish the influence of the background. By using a number of H_2O to CO_2 tran-

sitions to determine the concentration ratio of H_2O to CO_2 , the gas and oil products in the exhaust plume could be distinguished [6].

The capability of FTS to obtain accurate effluent concentration estimates from smokestack plumes has been demonstrated repeatedly since the 1970's. Prengle *et al.* used a Fourier-transform spectrometer based on a Michelson interferometer to demonstrate the potential for the remote sensing of pollutants such as CO , NO , NO_2 , unburned hydrocarbons, and combustion product olefins from sources such as power plants. Temperature and concentration models were developed and measurements of gas powered power plant plumes were made. It was shown that temperatures could be determined to within ± 10 K and concentrations estimated within 28% for concentrations in the $10 - 10^4$ ppm range [1]. Herget *et al.* used the remote optical sensing of emissions (ROSE) system to determine the pollutants in gas plumes. The ROSE system, a non-imaging Fourier-transform infrared system, was used to measure the emission and absorption spectra of the gas from a cement plant smokestack. The species observed were NO , CO , CO_2 , NH_3 , HCL , H_2CO , HF , and SO_2 . Temperature estimates were within 10% of *in situ* measurements, and concentrations were within 20% [4].

Research involving the use of FTS to study the spectra of turbulent plumes continued in the 1990's. Hilton *et al.* used an FTS to measure the emission spectra of a smokestack. These emission spectra were compared with those modeled using the HITRAN database to determine temperature and concentrations of CO_2 and H_2O in the plume. The temperature was determined to be $85 \pm 9^\circ\text{C}$, and the concentrations were accurate to within 10% [5]. The potential of using FTS to monitor smokestack emissions was also demonstrated by Haus *et al.* A high-resolution K300 spectrometer and a software based on radiative transfer line-by-line calculations and a least-squares method was used to estimate concentrations of smokestack and flare

plume emissions. FTS measurements were successfully performed of both power plant and small building smokestacks. The concentrations obtained from FTS were consistent with *in situ* measurements. For the case of power plant smokestacks, the average differences between FTS and *in situ* measurements seldom exceeded 25% [2]. FTS techniques have also been successfully applied in determining species concentrations of jet engine exhaust. Schaefer *et al.* demonstrated the capability of FTS to estimate plume effluent concentrations by comparing intrusive measurements of aircraft engine exhaust with those from an FTS. A spectroscopic database and software was developed to enable the determination of species concentrations. The results for CO₂, CO, and NO agreed with the intrusive measurements within 30%. A narrow-band device was used to obtain CO₂ concentration measurements, which agreed with the intrusive measurements within 10% [3]. Although past research demonstrates the capability of FTS to estimate species concentrations, discrepancies between FTS estimates and *in situ* measurements (between 10% and 30% difference in concentrations) suggests that the accuracy of these methods can be improved upon. Imaging FTS presents a means of improving upon traditional FTS methods.

2.1.2 Imaging Fourier-Transform Spectrometry of Turbulent Plumes.

While the study of turbulent plumes is not a new area of research, the use of imaging Fourier-transform spectrometers to observe plumes is an area still under development. Moore *et al.* used an IFTS to demonstrate that despite turbulent fluctuations, IFTS can be used to characterize the spectra of the exhaust plume of a turbojet engine. Temporal averaging was used to reduce SCAs in the spectra, and spatial maps of temperature and concentration were generated. The time-averaged spectra revealed clear CO and CO₂ emission features as well as information about plume temperature and concentrations. However, no information about the underly-

ing temperature distribution could be discerned [9].

Gross *et al.* showed the capability of using imaging Fourier-transform spectrometry to remotely monitor smokestack plumes. The Telops Hyper-Cam imaging spectrometer was used to obtain hyper-spectral imagery of a smokestack plume in order to study its chemical effluents and temperature. This data was time-averaged to reveal the discharge of HCl, CO₂, CO, SO₂, and NO. A single-layer plume radiative transfer model was applied to the pixels directly above the stack exit to estimate the temperature and column densities of the various constituents and observe how each varied across the plume. It was found that the temperature was fairly consistent across the stack with a mean of 396.3 ± 1.3 K and the effluent column densities fluctuated according to the plume pathlength. The estimated volume fractions of CO₂ ($8.6 \pm 0.4\%$) and SO₂ (380 ± 23 ppm_v) agreed well with *in situ* measurements ($9.40 \pm 0.03\%$ and 383 ± 23 ppm_v, respectively). NO was estimated to have a concentration of 104 ± 7 ppm_v. These results demonstrate the capability of using IFTS to not only identify various effluents, but also obtain accurate concentration estimates. Errors between *in situ* measurements and concentration estimates of SO₂ and CO₂ were 1% and 8%, respectively [7]. Although there was good agreement with *in situ* measurements, if and how much systematic error is introduced as a result of interpreting the time-averaged spectrum of a turbulent source is presently unknown. For example, because of the nonlinear effect of temperature fluctuations on the infrared spectrum, temperature fluctuations result in a time-averaged spectrum that cannot be described using the mean temperature alone. Instead, *a priori* knowledge of the underlying temperature probability density function (and the probability density functions of any other fluctuating parameters) is necessary to properly interpret the time-averaged spectrum.

A method of overcoming the effects of turbulent fluctuations in jet engine exhaust was demonstrated by Tremblay *et al.* This method involved statistically sort-

ing the data for each optical path difference (OPD) before performing a Fourier-transformation. Various quantiles of intensity were determined at each OPD and interferograms generated for each pixel. A Fourier-transform was then performed on the various quantile interferograms to obtain the corresponding spectra. After the quantile interferograms and spectra were constructed, spatial maps of the brightness temperature were created. Comparing the median and mean brightness temperature maps revealed sections of the plume where the mean and median differed considerably. Because of the nonlinearity of Planck's function, the mean is a biased estimate of brightness temperature for unsteady sources. Thus in turbulent sections of the plume, the mean spectrum could bias temperature (and consequently concentration) estimates. The results of this research demonstrate that using the median and other quantile interferograms, as opposed to the mean interferogram, result unbiased estimates of temperature [10].

2.2 Theory

Imaging Fourier-transform spectrometry combines the spectral information obtained from a Fourier-transform spectrometer with the spatial information of an imager. FTS uses an interferometer such as a Michelson to obtain the spectrum (radiance as a function of frequency) of a source. An IFTS combines a Michelson interferometer with an infrared camera to obtain an interferogram for each pixel in the focal plane array (FPA), or a series of images at successive OPDs. Taking the Fourier-transform of the interferogram at each pixel results in a series of spectral images at successive wavenumbers, or a spectrum at each pixel.

2.2.1 Fourier-Transform Spectrometry.

A traditional Michelson interferometer (see Figure 2 below) is based on a collimating lens, two mirrors (one stationary and one moving), a beamsplitter, and a detector. Light from the source is collimated by the lens and then divided by the beamsplitter into two components of equal amplitude. The two components are directed to separate mirrors and then reflected back by the mirrors to the beamsplitter. They are recombined again at the beamsplitter and directed to the detector. The two beams interfere with each other when recombined. The intensity seen by the detector is dependent upon the difference in the distances traveled by the two beams (optical path difference), controlled by the position of the moving mirror, as well as the spectrum of the source.

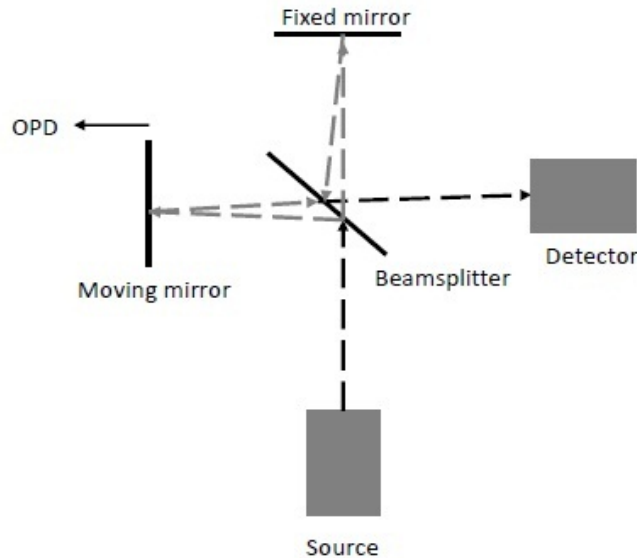


Figure 2. Diagram of a traditional Michelson interferometer. The intensity read by the detector is a function of the optical path difference of the two beams (controlled by the moving mirror) and the spectrum of the source.

The measured intensity as a function of OPD forms an interferogram. The intensity,

I_o , measured by the detector as a function of OPD for a monochromatic source is represented by

$$I_o(x_k) = L(\tilde{\nu}_o)[1 + \cos(2\pi\tilde{\nu}_ox)], \quad (1)$$

where x_k is the OPD, $L(\tilde{\nu}_o)$ is the spectral radiance, and $\tilde{\nu}_o$ is the wavenumber ($1/\lambda$). When source includes more than one frequency, the interferogram will be a superposition of cosine waves of different amplitudes and frequencies. The intensity is integrated up over all frequencies, resulting in Equation 2 below [12],

$$I_o(x_k) = \int_0^\infty L(\tilde{\nu})[1 + \cos(2\pi\tilde{\nu}x_k)]d\tilde{\nu}. \quad (2)$$

In non-imaging FTS, the mean (the spectral radiance, $L(\tilde{\nu})$, integrated over all frequencies) or DC component of intensity is removed, resulting in

$$I(x_k) = I_o(x_k) - I(\bar{x}_k) = \int_0^\infty L(\tilde{\nu})\cos(2\pi\tilde{\nu}x_k)d\tilde{\nu}. \quad (3)$$

Taking the Fourier-transform of Equation (3) gives the spectrum, or L as a function of $\tilde{\nu}$. For an interferogram extending from negative infinity to positive infinity, the cosine transform produces the monochromatic spectrum. The greater the frequency of the oscillations in the interferogram, the greater the frequency of the spectral line. In reality, the spectrum will not be monochromatic, but will correspond to a lower resolution due to the fact that a real interferogram is finite in length. The length of the interferogram is controlled by the maximum optical path difference of the instrument. The finite maximum optical path difference of the instrument gives rise to an instrument line shape (ILS) in the spectrum. This ILS is due to the truncation of the interferogram to a finite length, which is equivalent to multiplying it by a rectangular function or convolving the spectrum with a sinc function. An apodization function is used to reduce the “ringing” in the spectrum associated with

the sinc ILS side lobes by smoothly reducing the amplitude of the interferogram [12].

In imaging FTS, the DC component of intensity is retained, and a Fourier-transform of Equation 2 is taken. IFTS obtains a spectrum for each pixel, which can then be fit to a spectral model to obtain the temperature and effluent concentrations at each pixel in the plume.

2.2.2 Spectral Modeling.

Because a smokestack plume is not a perfect emitter and must radiate through the atmosphere before reaching the detector, the temperature of a pixel cannot simply be obtained from the spectrum through application of Planck's blackbody radiation law,

$$L(\tilde{\nu}) = \frac{2hc^2\tilde{\nu}^3}{e^{hc\tilde{\nu}/kT_B} - 1}. \quad (4)$$

Thus the spectra must be fit to a model to determine the kinetic temperatures in the plume. A spectral model describing the apparent radiance of the plume can be derived from the macroscopic radiative transfer equation,

$$\frac{dL(\tilde{\nu})}{ds} = -k_{\tilde{\nu}}(L(\tilde{\nu}) - S_{\tilde{\nu}}), \quad (5)$$

where $k_{\tilde{\nu}}$ is the extinction coefficient (which includes the effects of absorption and scattering of radiation) and $S_{\tilde{\nu}}$ is the source function (defined as the ratio of the emission coefficient to the extinction coefficient) [13].

Equation 5 can be written to include the effects of multiple scattering and absorption,

$$\frac{dL(\tilde{\nu})}{d\tau_{\tilde{\nu}}} = -L(\tilde{\nu}) + [1 - a(\tilde{\nu})]L_{BB}(\tilde{\nu}) + \frac{a(\tilde{\nu})}{4\pi} \int_{4\pi} d\Omega' p(\Omega', \Omega) L(\tilde{\nu})(\Omega'), \quad (6)$$

where $d\tau_{\tilde{\nu}} = k(\tilde{\nu})ds$ is the differential optical path, $a(\tilde{\nu})$ is the single scattering

albedo (the probability a photon will be scattered), $L_{BB}(\tilde{\nu})$ is the blackbody radiance, Ω is the direction of the radiative energy, and $p(\Omega', \Omega)$ is the scattering phase function. The thermal contribution of the source function is represented by $[1 - a(\tilde{\nu})]L_{BB}(\tilde{\nu})$, and the scattering component of the source function is represented by $\frac{a(\tilde{\nu})}{4\pi} \int_{4\pi} d\Omega' p(\Omega', \Omega) L(\tilde{\nu})(\Omega')$. In order to simplify the radiative transfer problem, it is assumed that scattering, background radiation, and self-emission from the atmosphere are minimal and that the plume is in local thermodynamic equilibrium (LTE). Since there is minimal scattering ($a(\tilde{\nu})$ is very small) and the plume is in LTE, the radiative transfer equation simplifies to

$$\frac{dL(\tilde{\nu})}{d\tau_{\tilde{\nu}}} = -L(\tilde{\nu}) + L_{BB}(\tilde{\nu}). \quad (7)$$

Solving the differential equation above with the assumption the plume is uniform along the line of sight yields

$$L(\tilde{\nu}, l) = L(\tilde{\nu}, 0)e^{-k_{abs}(\tilde{\nu})l} + (1 - e^{-k_{abs}(\tilde{\nu})l})L_{BB}(\tilde{\nu}, T), \quad (8)$$

where l represents the path length of the plume, $L(\tilde{\nu}, 0)$ is the background radiance, $k(\tilde{\nu})$ now includes only the absorption coefficient ($k_{abs}(\tilde{\nu})$) (since scattering is low), and $(1 - e^{-k_{abs}(\tilde{\nu})l})$ is the emissivity (1- transmittance) of the plume [13].

Ignoring background radiation, the apparent radiance at the boundary of the plume simplifies to

$$L(\tilde{\nu}, l) = \varepsilon L_{BB}(\tilde{\nu}, T). \quad (9)$$

Accounting for transmittance through the atmosphere to the detector and integrating over all wavenumbers, the radiance seen by the detector is represented by

$$L(\tilde{\nu}) = \int \tau(\tilde{\nu}') \varepsilon(\tilde{\nu}') L_{BB}(\tilde{\nu}', T) ILS(\tilde{\nu} - \tilde{\nu}') d\tilde{\nu}', \quad (10)$$

where τ is the atmospheric transmittance profile between the plume and the detector, and ILS is the instrument line shape function [7]. The convolution of the incident radiance with instrument line shape describes the instrument's resolving power. The instrument line shape is characterized by the shape of the spectral line (defined by the length and varying amplitude of the interferogram) and any apodization function used to reduce "ringing" [12].

The absorption coefficient for the j th absorption line of the i th species is defined as $k_{abs}(\tilde{\nu}) \equiv S_{i,j}N\Phi_{i,j}(\tilde{\nu})$, where $S_{i,j}$ is the line strength of the j th absorption line of the i th molecule, N is the total gas density (determined from the ideal gas law and the atmospheric temperature and pressure), and $\Phi_{i,j}(\tilde{\nu})$ is the profile of the j th line [13]. The emissivity can be rewritten by replacing $k_{abs}(\tilde{\nu})$ with $S_{i,j}N\Phi_{i,j}(\tilde{\nu})$ and summing over all lines for all species in the plume, resulting in

$$\varepsilon(\tilde{\nu}) = 1 - e^{-N \sum_i q_i \sum_j S_{i,j}(\tilde{\nu}_j, T) \Phi_{i,j}(\tilde{\nu}) \tau_p}, \quad (11)$$

where q_i is the fractional column density (volume fraction times the path length for the i th species), and τ_p is the transmittance of the soot in the plume. Near the center of the stack exit the path length is simply the stack diameter, and the volume fraction can be determined exactly [7].

The absorption cross-section for the i th species, $\sigma_i(\tilde{\nu}, T)$, is given by

$$\sigma_i(\tilde{\nu}, T) = \sum_j S_{i,j}(\tilde{\nu}_j, T) \Phi_{i,j}(\tilde{\nu}), \quad (12)$$

where $S_{i,j}$ is the line strength of the j th line for the i th molecule, and $\tilde{\nu}_j$ is the central wavenumber of the transition. The line strengths depend on the individual transition as well as the population in the ground state. Assuming LTE, the distribution of excited states is defined by the Boltzmann distribution, and $S_{i,j}$ depends explicitly

on the kinetic temperature of the plume. These line strengths can be determined theoretically or experimentally. The HITRAN database [11] includes the information needed to calculate the absorption cross-sections for the species present in the plume [13]. Using this information, the spectra can be fit to the spectral model (Equation 10) to determine temperatures and effluent concentrations.

2.2.3 Statistics Background.

The cumulative distribution function (CDF) describes the probability that a variable X is less than or equal to a value x and can be represented by $D(x) = P(X \leq x)$, where $D(x)$ represents the CDF. The probability density function (PDF) is defined as the derivative of the CDF, and describes the probability of obtaining a given value of X . For a normally distributed random variable, the CDF and PDF are represented by Figure 3, where Figure 3 has been standardized to a mean of 0 and a standard deviation of 1. A quantile is any point along the CDF. The Q th quantile represents the value of x such that there is a probability Q of obtaining a value less

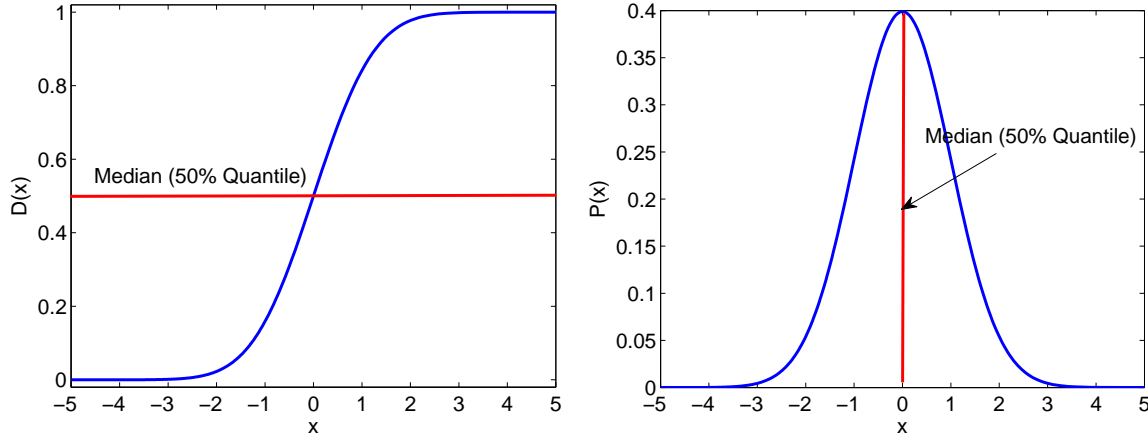


Figure 3. Cumulative distribution function (left) and probability distribution function (right) for the standard normal distribution, where $D(x)$ is the probability of obtaining a value less than or equal to x and $P(x)$ is the probability of obtaining a value equal to x .

than or equal to x . For example, the median (or 50%) quantile is the value of x with a 50% probability of obtaining a value less than or equal to it. Thus from a distribution of quantiles the CDF and consequently the PDF can be derived.

III. Understanding the Influence of Turbulence in Imaging Fourier Transform Spectrometry of Smokestack Plumes

3.1 Abstract

An imaging Fourier-transform spectrometer (IFTS) was used to collect infrared hyper-spectral imagery of smokestack plume associated with coal-burning power facility to assess the influence of turbulence on spectral retrieval of temperature (T) and pollutant concentrations (C_i). A mid-wave (1.5-5.5 μm) Telops Hyper-Cam was used and features a 320x256 InSb focal-plane array with a 326 μrad instantaneous field-of-view (IFOV). The line-of-sight distance to the 76 m tall smokestack exit was 350 m (11.4 x 11.4 cm^2 IFOV). Approximately 5000 interferogram cubes were collected in 30 minutes on a 128x128 pixel window corresponding to a spectral resolution of 20 cm^{-1} . Radiance fluctuations due to plume turbulence were observed on a time scale much shorter than hyper-spectral image acquisition rate, thereby introducing scene change artifacts (SCA) in the Fourier-transformed spectra. Time-averaging the spectra minimizes SCA magnitudes, but accurate T and C_i retrieval would require a priori knowledge of the statistical distribution of temperature and other stochastic flow field parameters. A method of quantile sorting in interferogram space prior to Fourier-transformation is presented and used to identify turbulence throughout the plume. It is demonstrated that if radiance fluctuations are due only to temperature fluctuations, the spectrum associated with each interferogram quantile directly corresponds to the corresponding quantile temperature. Analysis of the quantile spectra indicate that radiance fluctuations are driven by more than just temperature fluctuations. Immediately above the stack exit, T and CO_2 concentration estimates from the median spectrum are 395 K and 6%, respectively, which compare well to *in situ* measurements. Turbulence is small above the stack exit and introduced systematic

errors in T and C_i on the order of 0.5 K and 0.01%, respectively. In some plume locations, turbulent fluctuations introduced errors in T and C_i on the order of 8 K and 1%, respectively. While more complicated radiance fluctuations precluded straightforward retrieval of the temperature probability distribution, the results demonstrate the utility of additional information content associated with multiple interferogram quantiles and suggest IFTS may find use as a tool for non-intrusive flow field analysis.

3.2 Introduction

Fourier-transform spectrometry (FTS) has long been employed for the remote characterization of the spectra of chemical plumes. The ability to determine with confidence the species concentrations emitted from a smokestack without the need for *in situ* measurements has important intelligence and governmental applications. FTS presents the opportunity to remotely monitor smokestacks to verify adherence with environmental regulations without disruption of plant operations. The ability to simultaneously determine the concentrations of multiple chemical species make FTS an attractive option for the purpose of monitoring smokestack emissions. Its mobility, distance from the source, and the fact that FTS is a passive technique all provide the potential to monitor smokestacks undetected, making FTS advantageous for monitoring smokestack effluents for intelligence purposes as well. While previous research has demonstrated the capability of using non-imaging FTS to characterize plumes [1]-[6], the degree to which turbulence in smokestack plumes affects spectral interpretation is unknown. The accuracy of effluent concentrations obtained by non-imaging FTS can be improved upon by imaging Fourier-transform spectrometry (IFTS), which provides the additional spatial advantage over non-imaging FTS. Non-imaging FTS lacks the ability to isolate specific regions of the source, and the results can be affected by incorporating both turbulent and steady regions of the source or regions other than

the source itself. IFTS possesses the ability to isolate specific regions of the plume and improve the accuracy of effluent concentration estimates. Because IFTS retains the DC component of intensity, which is removed in virtually all non-imaging FTS, the spectra can be statistically sorted into quantile spectra. These quantile spectra provide additional information related to flow field fluctuations.

While IFTS is an efficient means for the remote characterization of a static source, problems arise when observing a turbulent source such as a smokestack plume. Turbulence due to temperature or concentration fluctuations in the plume introduces scene change artifacts (SCAs) which corrupt the spectra. Figure 4 shows images (0.1 seconds apart) captured with the Telops Hyper-Cam imaging spectrometer and shows the structure of the plume changing with time. These images demonstrate the presence of turbulent fluctuations in the plume, which must be taken into account to gain better confidence in effluent concentration estimates obtained by IFTS.

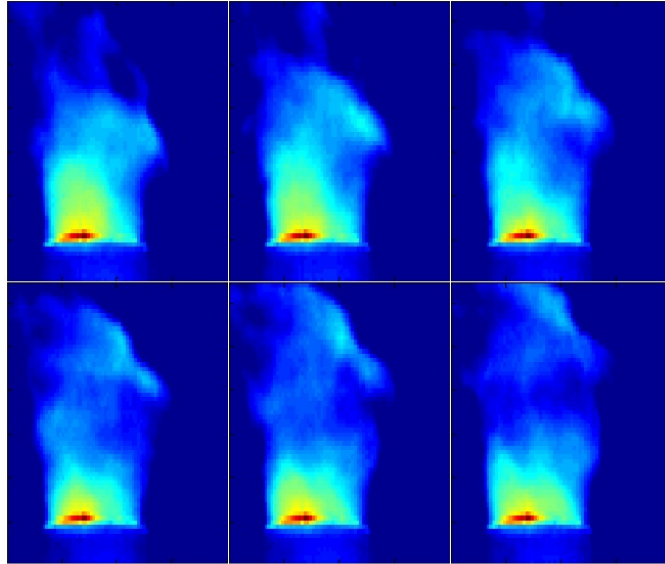


Figure 4. Images of a coal-burning smokestack plume changing with time captured with the Telops Hyper-Cam imaging spectrometer. The presence of turbulent fluctuations is apparent in the changing structure of the plume.

Because the radiative transfer model used to determine temperatures and effluent concentrations assumes a single temperature source, accurate interpretation of the spectra requires an understanding of the underlying temperature distribution. Non-linearities in the spectral model result in a bias of temperatures (and hence concentrations) retrieved from the time-averaged spectrum. Thus knowledge of the underlying temperature distribution is required to accurately simulate the time-averaged spectrum. If both temperature and effluent concentrations are fluctuating, then knowledge of both the temperature and concentration distributions is necessary.

This research uses hyper-spectral imagery of a coal-burning smokestack plume obtained from the Telops Hyper-Cam imaging spectrometer to quantify the effects of turbulence on the proper interpretation of smokestack emissions for accurate pollutant concentration retrieval. In past studies, it has been shown that IFTS can be used to determine the effluents and concentrations of a turbulent source by reducing spectral artifacts through temporal averaging [7]-[9]. However, due to non-linearities in the model, use of the mean spectrum gives a biased estimate of temperature (and therefore concentrations). This research seeks to use a single-layer radiative transfer model to estimate temperature and column densities for each plume pixel. A novel method of processing the interferograms is employed that reduces spectral artifacts and under the correct conditions provides unbiased temperature and column density estimates. This method provides a means of understanding the effect of turbulence throughout the plume by leveraging the DC level imagery to produce quantile interferograms. Assuming only temperature is causing turbulent radiance fluctuations, quantile spectra can be mapped to corresponding quantile temperatures and the underlying temperature distribution discerned. This research seeks to use these quantile spectra to quantify the turbulence-driven radiance fluctuations and determine if temperature fluctuations are in fact the primary cause. This also enables the estimation

of retrieved concentration confidence bounds which include the effects of turbulence. The potential of IFTS for general non-intrusive analysis of emissive flow fields is also demonstrated. IFTS, because it retains the DC component of intensity, provides quantile spectra which contain fluctuation information across the plume. A simulation tool for modeling mid-wave infrared spectra of turbulent gas-phase sources is also developed.

3.3 Methodology

Previous work using IFTS to characterize the exhaust plume of a turbojet engine showed that turbulent fluctuations introduced SCAs into the spectrum, which were treated as noise and reduced through temporal averaging. Although the signal-to-noise ratio was increased and spectral emission lines were identified, no information about underlying temperature distribution could be discerned [9]. Previous research involving IFTS of smokestack plumes also used time-averaged spectra, and concentration estimates agreed well with *in situ* measurements [7]. However the degree to which use of the mean spectra biased these results is unknown. Another method of processing the interferograms that offers unbiased estimates of temperature and concentration as well as information about underlying temperature distribution is presented. Application of this method can increase confidence in concentrations of smokestack effluents obtained by IFTS.

3.3.1 IFTS.

The intensity detected by the instrument can be represented by

$$I(x_k) = \int_0^\infty (1 + \cos(2\pi x_k \tilde{\nu})) L(\tilde{\nu}; t(x_k)) d\tilde{\nu} = I_{DC} + I_{AC}, \quad (13)$$

where x_k is the optical path difference (OPD), $\tilde{\nu}$ corresponds to the wavenumber ($1/\lambda$), $L(\tilde{\nu}, t(x_k))$ is the time-varying spectral radiance, and $t(x_k)$ is the time of the sample at x_k . In this work, it is assumed that at time $t(x_k)$, each physical parameter which affects the radiance is taken from an appropriate distribution function. The simple case in which only temperature fluctuations are present will be considered. The intensity as shown in Equation 13 can be split into two pieces, I_{DC} and I_{AC} . I_{DC} is simply $L(\tilde{\nu}, T)$ integrated over all wavenumbers and will be constant for a static source. In nearly all non-imaging FTS, I_{DC} is removed prior to analog-to-digital conversion using an electronic high-pass filter. I_{AC} is the modulated piece and is associated with the cosine transform of $L(\tilde{\nu}, T)$. Taking the Fourier-transform results in the raw spectrum, which can then be calibrated to radiance units [10].

3.3.2 Spectral Model.

In order to determine temperature and effluent concentrations across the plume, the spectra are fit a model, represented by

$$L(\tilde{\nu}) = \int \tau(\tilde{\nu}') \varepsilon(\tilde{\nu}') L_{BB}(\tilde{\nu}', T) ILS(\tilde{\nu} - \tilde{\nu}') d\tilde{\nu}', \quad (14)$$

where $L(\tilde{\nu})$ corresponds to the apparent spectral radiance, τ is the atmospheric transmittance profile between the plume and the detector, ε represents the spectral emissivity of the plume, L_{BB} is Planck's blackbody radiance, and ILS represents the instrument line shape (characterized by the shape of the spectral line as well as any apodization function used) [13].

The spectral emissivity is determined from

$$\varepsilon(\tilde{\nu}) = 1 - e^{-\sum_i q_i N \sigma_i(\tilde{\nu}, T)} \tau_p, \quad (15)$$

where q_i (the fractional column density) is the volume fraction times the path length for the i th species, N is the total gas density, σ_i is the absorption cross-section (calculated from information contained in the HITRAN database [11]), and τ_p is the transmittance of the soot in the plume [13]. The total gas density is given by the ideal gas law, $N = \frac{P}{k_B T}$, and hence N is also dependent upon temperature. Because the relative populations of each molecule's internal energy states are defined by the Boltzmann distribution, σ_i is also a function of temperature.

Spectral fitting was accomplished by first computing the absorption cross-sections for the various plume effluents, CO_2 , CO , SO_2 , HCl , H_2O , using the Line By Line Radiative Transfer Model (LBLRTM) [14]. LBLRTM was used to calculate the absorption cross-sections at 1 K increments for the temperature range of the plume from spectral line data contained in the HITRAN database [11]. Linear interpolation was used to determine the absorption cross-sections for temperatures in between.

A radiative transfer model (Equation 14) was then used to compute the apparent radiance of the plume. The parameters for modeling atmospheric transmittance were atmospheric temperature, CO_2 concentration, relative humidity, pathlength, and pressure. The parameters varied in the model were temperature (T), fractional column density of CO_2 (q_{CO_2}), and soot transmittance (τ_p). Because the plume pathlength is known only above the stack exit, CO_2 concentration is reported in terms of column density. Due to the low spectral resolution, CO_2 was the only species with notable spectral features and thus was the only species included in the model. The other species in the plume were held constant and assumed to be known. Increasing the spectral resolution (at the expense of data size and processing time) would allow other species in the plume to be resolved.

Use of a monochromatic radiative transfer model is computationally expensive. Therefore a spectral interpolation method was devised in order to make fitting each

quantile spectrum for each pixel feasible. The radiative transfer model was used to compute the apparent radiance for a range of the three variables, T , q_{CO_2} , and τ_p . This was done for each wavenumber sampled and resulted in a three-dimensional matrix for each wavenumber on the spectral axis. A model for spectral fitting was then created from this array through linear interpolation of the in-between parameter values. This model eliminated the need to perform the calculations using the radiative transfer model during the spectral fitting process. The data was fit to the interpolation model by employing a Neider-Mead search followed by a Levenberg-Marquardt nonlinear minimizer. Because the only species modeled was CO_2 , only the 2000 to 2450 cm^{-1} region was included in the fit. The mean as well as the Q_{med} , $Q_{\pm 0.5s}$, $Q_{\pm 1s}$, $Q_{\pm 1.5s}$ and $Q_{\pm 2s}$ spectra were fit to the spectral model.

For turbulent sources, the various flow field parameters (such as temperature, species concentrations, density, and velocities) will fluctuate randomly about their mean values. To simplify the discussion, it is assumed that only temperature fluctuations affect the time-averaged spectrum. If temperature is fluctuating, proper interpretation of the spectra requires some knowledge of the underlying temperature distribution, which is not provided by the time-averaged spectrum. The radiative transfer model used to fit the data and determine temperature and effluent concentrations is a single temperature model. In other words, the model assumes that the source is steady (i.e. the temperature distribution is a delta function) and therefore that the average radiance is the radiance at the average temperature. When the temperature of the source is varying, there will be a temperature probability density function with some shape and width and the model breaks down. The average radiance of the source if temperature is fluctuating is represented by

$$\langle L(\tilde{\nu}) \rangle = \int P(T) L_{model}(\tilde{\nu}, T) dT, \quad (16)$$

where $\tilde{\nu}$ is wavenumber ($1/\lambda$), $\langle L(\tilde{\nu}) \rangle$ is the average spectral radiance, $P(T)$ represents the temperature probability density function, and $L_{model}(\tilde{\nu}, T)$ is the model radiance (represented by Equation 14). Because temperature fluctuates according to some underlying distribution, L_{model} must be weighted by the probability of obtaining a specific temperature. Knowledge about the temperature distribution provides an understanding of the fluctuation strength and can increase the confidence in the temperature and concentrations provided by the model. The closer the temperature distribution is to a delta function (i.e. the steadier the source), the more accurate the single temperature model approximation. The method presented utilizes the median and other quantiles to discern the nature of the temperature distribution and is based on the assumption that temperature is the only parameter fluctuating.

3.3.3 Turbulent Sources.

IFTS relies on the assumption that the source under observation is constant. For a turbulent source with fluctuations in radiance that are purely a result of temperature fluctuations, the temperature fluctuates from one OPD to the next, appearing as “noise” in the interferogram. This introduces spectral artifacts and corrupts the spectra. Time-averaging results in a spectrum with few SCAs, however proper interpretation of this spectrum requires knowledge of the underlying temperature distribution. Use of a single temperature model to retrieve the temperature will produce biased results due to inherent nonlinearities in the model. For example, there is a non-linear relationship between temperature and blackbody spectral radiance in Planck’s function,

$$L_{BB}(\tilde{\nu}) = \frac{2hc^2\tilde{\nu}^3}{e^{hc\tilde{\nu}/kT_B} - 1}, \quad (17)$$

where T_B corresponds to the brightness temperature, $\tilde{\nu}$ corresponds to the wavenumber in cm^{-1} , h is Planck’s constant, c is the speed of light, k is Boltzmann’s con-

stant, and $L_{BB}(\tilde{\nu})$ is the blackbody spectral radiance. Because of the nonlinearity of Planck's function, the average $L_{BB}(\tilde{\nu})$ of a temperature-fluctuating blackbody is not the $L_{BB}(\tilde{\nu})$ associated with the mean T_B , and is actually not a blackbody spectral radiance at any temperature. The effect is the same when considering the average model radiance, which includes the blackbody spectral radiance. The average model radiance is not equal to the radiance at the the average temperature,

$$\langle L(\tilde{\nu}) \rangle = \int P(T) L_{model}(\tilde{\nu}, T) dT \neq L_{model}(\tilde{\nu}, \langle T \rangle). \quad (18)$$

Therefore fitting the time-averaged spectrum to the spectral model results in a biased estimate of temperature (and hence concentration), and accurate interpretation of the spectra requires knowledge of the underlying temperature distribution. Median and other quantile spectra, however, provide unbiased estimates of temperature. The median temperature will therefore be the temperature retrieved from the median spectrum. In addition to providing unbiased temperature and concentration estimates, quantile spectra can also provide additional information regarding the underlying temperature distribution.

3.3.4 Quantile Analysis Method.

This method involves sorting the interferograms into quantiles prior to taking the Fourier-transform. The monotonic relationship between temperature and intensity enables each quantile interferogram to be mapped to a single quantile temperature and the underlying temperature distribution retrieved. It can be shown that there is a monotonic relationship between the blackbody radiance and temperature [10]. The plume radiance, which includes the blackbody radiance, can also be shown to be monotonic with temperature. Figure 5 shows the model radiance, $L(\tilde{\nu}, T)$, at a temperature of 390 K subtracted from the model radiance at 400 K. Because the dif-

ference the two spectra is greater than zero at all wavenumbers, the spectral radiance in Figure 5 increases with temperature at all wavenumbers. This demonstrates the monotonicity of $L(\tilde{\nu}, T)$ with temperature for the chosen temperatures. This assumption that spectral radiance is monotonic with temperature was verified for the range of temperatures expected in the plume.

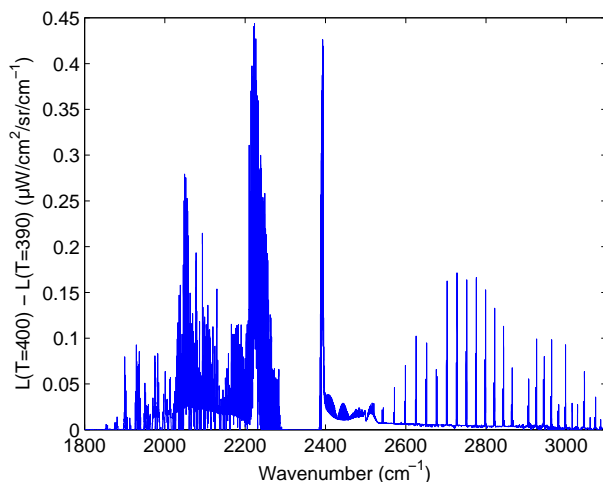


Figure 5. Difference in the model radiance at two temperatures: $L(\tilde{\nu}, 400K) - L(\tilde{\nu}, 390K)$. $L(\tilde{\nu}, 400K) - L(\tilde{\nu}, 390K)$ is greater than zero at all wavenumbers.

Because the unmodulated component of intensity, I_{DC} , is maintained, there is also a monotonic relationship between the total intensity and the spectral radiance. Since $L(\tilde{\nu}, T)$ in Equation 13 is weighted by a number that is always positive ($1 + \cos(2\pi x_k \tilde{\nu}) \geq 0$) and $L(\tilde{\nu}, T)$ increases monotonically with temperature at all wavenumbers, the intensity also increases monotonically with temperature. Assuming the temperature fluctuates rapidly compared to the time between samples and concentration fluctuations are small, sampling the intensity at a specific OPD corresponds to sampling a single temperature from the temperature probability density function.

Since $L(\tilde{\nu}, T)$ and $I(x_k)$ are both monotonic functions with the source tempera-

ture, the various quantiles are maintained when converting from one to the next,

$$\begin{aligned}
Q &= P\{T \leq T_Q\}, \\
&= P\{L(\tilde{\nu}, T) \leq L(\tilde{\nu}, T_Q)\}, \forall \tilde{\nu}, \\
&= P\{I(x_k) \leq I_Q(x_k)\}, \forall x_k,
\end{aligned} \tag{19}$$

where Q is the quantile with a probability Q of $T \leq T_Q$ and $I_Q(x_k)$ the intensity at the Q th quantile. This monotonic relationship implies that by sampling a large enough number of interferograms, a representative portion of the underlying temperature distribution has also been sampled. If a large number of interferograms are collected, the intensity at a specific OPD can be found for each interferogram and the underlying intensity distribution at that OPD retrieved. Various intensity quantiles can be found for each OPD and quantile interferograms that are free from SCAs constructed. This can be done for any number of quantiles. Because the DC component of intensity is preserved, each quantile interferogram corresponds to a single quantile temperature. This method cannot be applied, however, to non-imaging FTS. Because I_{DC} is filtered out in traditional Fourier-transform spectrometers, the monotonic relationship between the observed intensity and $L(\tilde{\nu}, T)$ breaks down. The quantile interferogram for the Q th quantile is represented by Equation 20 below [10],

$$I_Q(x_k) = \int_0^\infty (1 + \cos(2\pi\tilde{\nu}x_k)L(\tilde{\nu}, T_Q)d\tilde{\nu}. \tag{20}$$

Note that if both concentration and temperature experience large fluctuations, then a specific intensity corresponds to sampling from a probability density function of both variables. In this case, quantile interferograms cannot be mapped to a single temperature. However the various quantile interferograms (and their corresponding quantile spectra) still contain information that may be useful in understanding the

nature of the source turbulence.

A discrete Fourier-transform is taken of Equation 20 to obtain quantile spectra. The corresponding kinetic temperatures and effluent concentrations are obtained by fitting the spectra to the spectral model. The temperature quantiles can be used to derive the temperature cumulative distribution function, from which the temperature probability density function can be obtained. Taking the difference between two temperature quantiles gives an estimate of the standard deviation and provides a measure of quantifying the temperature fluctuations in the plume. While the method of sorting the interferograms still holds, if the concentration fluctuates along with the temperature, then the monotonic relationship between intensity and temperature breaks down and a specific intensity corresponds to sampling from a distribution of both temperature and concentration. A quantile spectrum will correspond to a range of temperature and concentration pairs rather than to single temperature.

When statistically sorting the interferograms, accommodations had to be made for the large size of the data cubes. One row from each data cube was imported at a time. After importing the row from all data cubes, the desired quantiles for that row were determined. The quantiles were determined one row at a time until quantile spectra for each pixel in the plume were generated. When computing the mean interferogram, however, an entire data cube was imported at a time and added to the previous data cubes. Dividing by the total number of data cubes at the end generated the mean interferogram. Thus simply time-averaging the interferograms is less computationally expensive than sorting interferograms into quantiles.

3.4 Experimental

3.4.1 Stack Measurements.

A coal-burning industrial smokestack near Dayton, Ohio was observed the evening of 20 August, 2010 using the Telops Hyper-Cam, a mid-wave infrared imaging Fourier-transform spectrometer. The plant has three smokestacks approximately 76 m tall, and measurements were taken of the center stack (the only stack operating). The instrument was set up 350 m from the top of center stack (determined using a Newcon Optik LRB3000 Pro laser range finder), and data was taken for approximately 30 minutes. The goal of the test was to collect hyper-spectral imagery of the smokestack plume for the characterization of turbulence within the plume. Measurements were taken with a high enough spatial resolution to capture the strong fluctuations in radiance and a low enough spectral resolution so that a large enough sample of data cubes for statistical analysis could be taken in a reasonable time frame. Measurements were performed in the evening to reduce the effect of background radiation.

In order for sufficient spatial resolution of the turbulent fluctuations, the distance of the instrument to the smokestack was chosen such that each pixel viewed relatively small sections of the plume. The instrument was set up about 350 meters from the stack, resulting in a field of view (FOV) of $11.4 \times 11.4 \text{ cm}^2$ for each pixel. Figure 6 shows the location of the smokestack under observation along with the location of the observation point. The location was chosen so that the instrument could be set up far enough from any sources of noise (such as the generators used to power the equipment) and the potential of objects entering the field of view (FOV) of the instrument was minimal.

Hyper-spectral imagery was collected in the evening from approximately 1:26 am UTC to 2:15 am UTC with a moderately cloud covered sky background. Meteorological measurements were taken with a Kestrel 9500. During data collection the average

ambient temperature was 23.8°C, the average humidity was 75.4%, the average atmosphere pressure was 991.8 hPa, and the wind speed was 3.5 mph from the SSE direction.

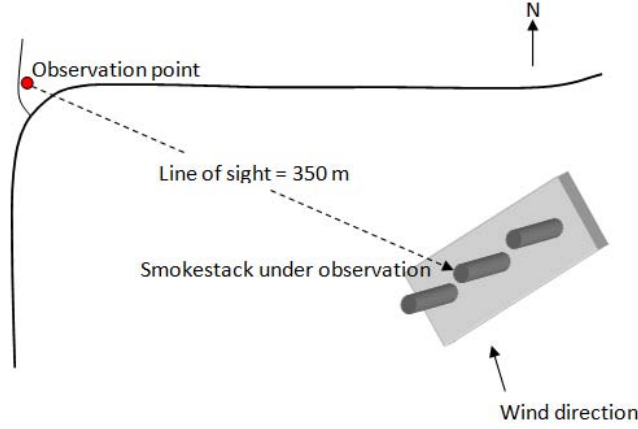


Figure 6. Diagram of the coal-burning power plant and test observation point.

3.4.2 Instrumentation.

The Telops Hyper-Cam operates using a Michelson interferometer to obtain a two-dimensional image of a source's intensity for many successive OPDs, resulting in an interferogram cube. The instrument has a 320 x 256 pixel 16-bit Stirling-cooled InSb focal plane array (FPA) and a spectral range of 1800-6667 cm^{-1} . The spectral resolution ranges from 0.25-150 cm^{-1} . Each pixel has an instantaneous FOV of 0.326 mrad. The spectral resolution, FOV, and integration time can all be adjusted to improve the acquisition rate. The instrument was configured with a FOV of 128 x 128 pixels. The spectral resolution was 20 cm^{-1} . Using a 90 μs integration time, 5048 data cubes were collected in approximately 30 minutes. Due to the large size of the data cubes and the corresponding time required to process the data cubes, only one 30 minute test was performed.

Two internal blackbodies of known temperature were used for the radiometric cal-

ibration of the raw spectra. These blackbody measurements provide the information needed to calculate the gain and offset coefficients used to convert raw spectra to radiance units. Blackbody temperatures were chosen that resulted in intensities that closely bracketed the range of digital numbers of the plume. The higher calibration temperature was chosen such that the FPA would not saturate. Calibration data was collected at temperatures of 20°C and 45°C, spectral resolution of 20 cm⁻¹, and an integration time of 90 μs. 500 data cubes were collected at each temperature. Calibration was performed by first converting the interferograms into raw spectra. The calibration temperatures, 318.05 K and 292.61 K, were then converted into radiance units in order to take advantage of the linear relation between digital number and radiance. The gain and offset coefficients were then found and the raw spectra converted to radiance units [W/(cm²·sr·cm⁻¹)]. A minimum wavenumber of 1750 cm⁻¹ and a maximum of 3000 cm⁻¹ were used. A hamming apodization function and phase correction were applied.

3.5 Results and Discussion

The data set analyzed consisted of 2524 data cubes with a spectral resolution of 20 cm⁻¹ and a FOV of 128 x 128 pixels. Because the data in forward and reverse scan directions must be analyzed separately, only half the data collected was analyzed. The raw interferograms were sorted into various quantile interferograms corresponding to cumulative probabilities of 0.023, 0.067, 0.159, 0.309, 0.5, 0.692, 0.841, 0.933, and 0.977. For a Gaussian distribution, these cumulative probabilities correspond to the median, ±0.5s, ±1s, ±1.5s and ±2s quantiles (Q_{med} , $Q_{\pm 0.5s}$, $Q_{\pm 1s}$, $Q_{\pm 1.5s}$ and $Q_{\pm 2s}$) quantiles, where s represents the standard deviation. These interferograms were then converted to spectra and calibrated to radiance units. However, due to the low probability of observing events outside ±1s, estimates of the true quantiles outside

of $\pm 1s$ will likely be poor.

3.5.1 Spectral Imagery.

When fitting data to a spectral model, the mean or median spectrum can be used to obtain temperature and concentration estimates. For a steady source, the mean and median spectra will be equal and simply time-averaging the spectra is sufficient for accurate temperature and concentration estimates. Figure 7 below demonstrates the difference between the mean and median spectra. The top left image in Figure 7 corresponds to the mean radiance ($L_{mean}(\tilde{\nu})$) [$\mu\text{W}/\text{cm}^2/\text{sr}/\text{cm}^{-1}$] at 2238 cm^{-1} , a strong CO_2 emission feature, and appears similar to the median radiance ($L_{med}(\tilde{\nu})$) at 2238 cm^{-1} . The area above the stack exit, where $L_{mean}(\tilde{\nu})$ is on the order of $1\text{ }\mu\text{W}/\text{cm}^2/\text{sr}/\text{cm}^{-1}$, corresponds to the area of greatest temperature. As the plume spreads out and decreases in temperature, $L_{mean}(\tilde{\nu})$ decreases. Because Figure 7 corresponds to a strong CO_2 emission feature, the plume radiance (approximately $1\text{ }\mu\text{W}/\text{cm}^2/\text{sr}/\text{cm}^{-1}$ above the stack exit) is much greater than that of the stack (approximately $0.3\text{ }\mu\text{W}/\text{cm}^2/\text{sr}/\text{cm}^{-1}$), which is nearly imperceptible compared to the background. The image in the top right corresponds to the mean spectra at several pixels in different areas of the plume as well as in the background and stack. Pixel (15, 70), corresponding to the stack, exhibits continuum emission consistent with radiation from a graybody with emissivity 0.12 and temperature 375 K. Pixel (35, 125) corresponds to background radiation and is much less than that of the bright plume pixels. Pixel (35, 65) corresponds to the brightest region above the stack, resulting in the spectrum with the largest spectral features. Pixel (62, 61) is located in the center of the plume, pixel (68, 89) is located in a more turbulent section in the right edge of the plume, and pixel (118, 16) is located in the area of lower $L_{mean}(\tilde{\nu})$ in the top left of the image. The largest peaks in the plume spectra, most noticeable at

pixel (35, 65), occur as a result of the P and R branches corresponding to transitions between different CO₂ vibrational levels [7]. The emission feature peaking at 2068 cm⁻¹ results from a combination of different CO₂ rotational-vibrational transitions. The emission features at 2392 cm⁻¹ (commonly called the red spike) and 2238 cm⁻¹ (commonly called the blue spike), most of which would normally be absorbed by atmospheric CO₂, arise from increased populations in higher-energy rotational levels caused by high plume temperatures [7].

Although the mean and median radiance ($L_{med}(\tilde{\nu})$) images would appear nearly identical, Figure 7 demonstrates the differences between the mean and median. The bottom left image in Figure 7 corresponds to $L_{mean}(\tilde{\nu}) - L_{med}(\tilde{\nu})$ [$\mu\text{W}/\text{cm}^2/\text{sr}/\text{cm}^{-1}$] at 2238 cm⁻¹. For a perfectly steady source, $L_{mean}(\tilde{\nu})$ and $L_{med}(\tilde{\nu})$ would be the same. However, Figure 7 shows differences between the mean and median, the greatest being on the outer right edge of the plume. The bottom right image in Figure 7 corresponds to the difference between the spectra at the same pixels as those shown in the mean spectra image. The difference between the spectra is the greatest for those pixels in the plume, with the largest difference appearing in pixel (68, 89). The greatest differences occur at emission features in the plume spectra. The difference between the mean and median is near zero for the pixels located in the stack and background, as would be expected for steady sources, and near zero at the stack exit. The difference between the mean and median spectra indicates the presence of radiance fluctuations in the plume, the source of which could be due to turbulent temperature or concentration fluctuations in the plume or some other phenomenon such as wind. The validity of the assumption that temperature is the primary of cause of turbulent radiance fluctuations can be investigated by fitting the spectra to the model. Even though Figure 7 demonstrates $L_{mean}(\tilde{\nu})$ and $L_{med}(\tilde{\nu})$ appear to be nearly equal at the stack exit, there are some fluctuations and the mean spectrum could still introduce a bias

into the fit results. The severity of this bias can be investigated by comparing the mean and median fit results.

3.5.2 Fit Results.

Fitting the data to the spectral model yielded residuals that exhibited some structure. Figure 8 shows the mean and median fit and residuals for several pixels in the

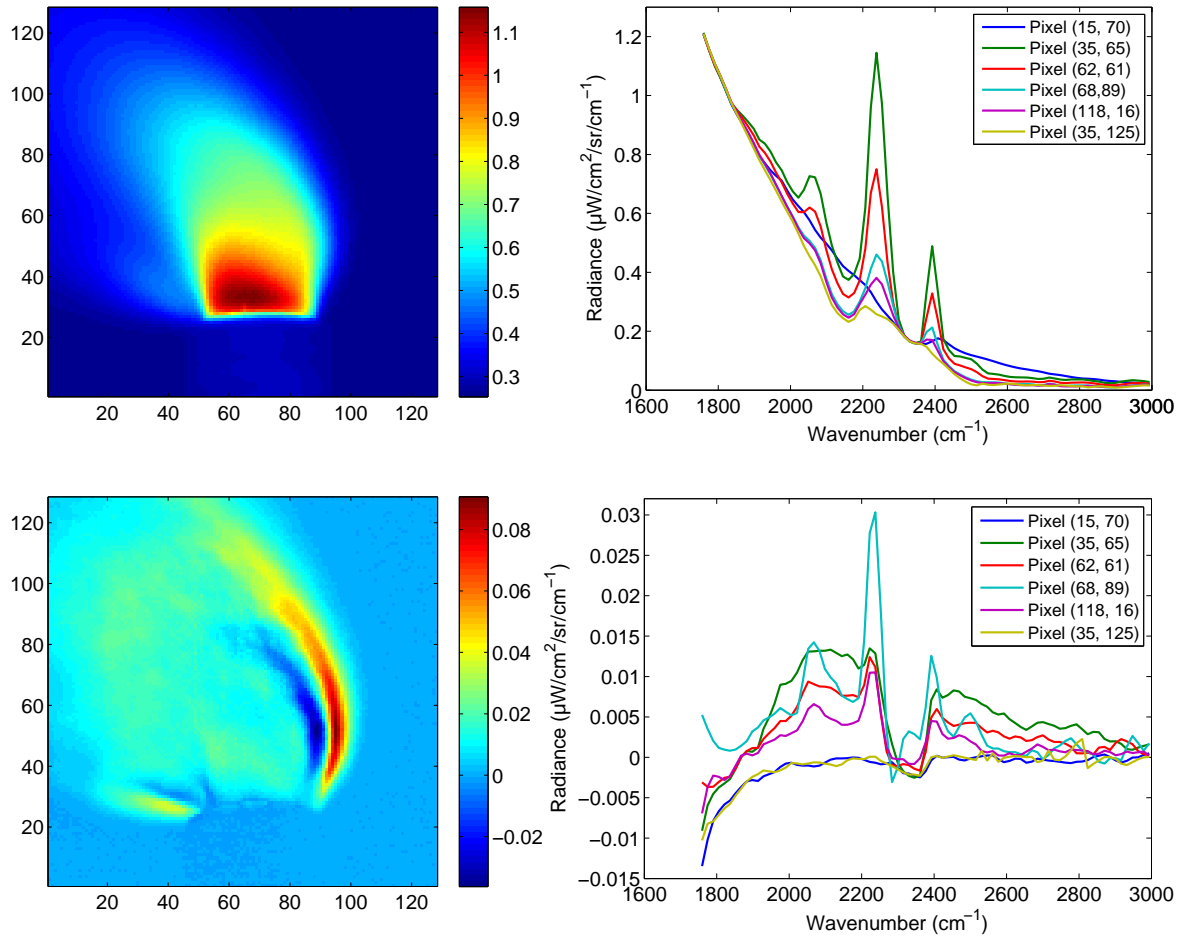


Figure 7. Top left: $L_{mean}(\tilde{\nu})$ [$\mu\text{W}/\text{cm}^2/\text{sr}/\text{cm}^{-1}$] at 2238 cm^{-1} , a CO_2 emission feature. Top right: Mean Spectra at several pixels corresponding to the stack, plume, and background radiation. The large spectral features correspond to CO_2 emission features due to rotational-vibrational transitions. Bottom left: $L_{mean}(\tilde{\nu}) - L_{med}(\tilde{\nu})$ [$\mu\text{W}/\text{cm}^2/\text{sr}/\text{cm}^{-1}$] at 2238 cm^{-1} . Bottom right: Mean - median spectra at several pixels corresponding to the plume, stack, and background radiation.

plume, (35, 65), (62, 61), (68, 89), and (118, 16). The model and data are shown for only the 2000 to 2450 cm^{-1} range, corresponding to the portion of the spectrum included in the fit. The structure in the residuals demonstrates the potential problems with the current spectral model. The residuals are also as much as an order of magnitude greater than the instrument noise level ($0.0013 \mu\text{W}/\text{cm}^2/\text{sr}/\text{cm}^{-1}$), indicating there to be significant systematic errors in portions of the plume. Although the mean and median data and fits appear very close, the greatest difference between the mean and median appears in pixel (68, 89), located in the turbulent right hand edge of the plume.

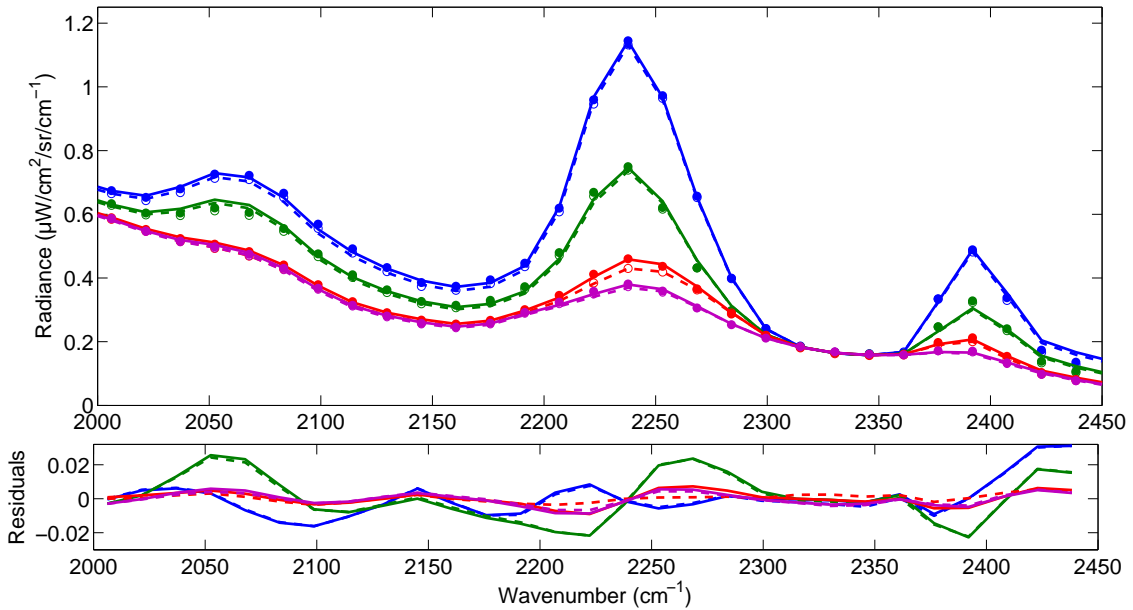


Figure 8. Top: Mean spectral data (solid circles), mean fit results (solid lines), median spectral data (empty circles), and median fit results (dashed lines) for pixels (35, 65) (blue), (62, 61) (green), (68, 89) (red), and (118, 16) (purple). Only the range included in the fit (2000 to 2450 cm^{-1}) is shown. Bottom: Residuals for the mean (solid lines) and median (dashed lines) for pixels (35, 65) (blue), (62, 61) (green), (68, 89) (red), and (118, 16) (purple).

The left hand image in Figure 9 represents a measure of the magnitude of the sys-

tematic error (R) throughout the plume, where $R = \langle (L_{mean}(\tilde{\nu}) - L_{model}(\tilde{\nu}))^2 \rangle$. The R_{mean} image, which is similar to that of the R_{median} image, shows a pattern of greatest error (approximately $0.014 \mu\text{W}/\text{cm}^2/\text{sr}/\text{cm}^{-1}$) in the center of plume. In this region, R_{mean} is an order of magnitude greater than the noise level of instrument, indicating the presence of systematic errors in the fit. This pattern of larger error in the center of plume is likely due to limitations in the model. The spectral model assumes the plume is uniform along the line of sight. However, Papanicolaou and List demonstrated in their measurements of axisymmetric plumes that the mean velocity and concentration profiles across the radius of the plume can be closely approximated by Gaussian profiles [15]-[16]. This implies that systematic errors in the plume are due to inhomogeneities along the line of sight. The line of sight in the edges of the plume in Figure 9 includes only the tails of the Gaussian concentration profile. The edges of the plume have had more time to mix with the surrounding atmosphere, and thus are more uniform along the line of sight. Because IFTS gives a two-dimensional representation of a three-dimensional source, the center of the image includes both the cooler, well-mixed edges of the plume as well as the warmer center. In the center of the image, the line of sight includes the entire Gaussian profile and is therefore is less uniform, resulting in a greater R . Although the largest R_{mean} is on the order of $0.014 \mu\text{W}/\text{cm}^2/\text{sr}/\text{cm}^{-1}$ (in the center of the plume), $L_{mean}(\tilde{\nu})$ in this region ranges from approximately 0.6 to $0.9 \mu\text{W}/\text{cm}^2/\text{sr}/\text{cm}^{-1}$. However the spatial pattern in the R_{mean} demonstrates the inadequacy of the current spectral model.

The systematic error related to just the turbulent fluctuations in the plume is captured in the right hand image in Figure 9. This error is represented by $R_{mean} - R_{median}$, which corresponds to $\langle (L_{mean}(\tilde{\nu}) - L_{model}(\tilde{\nu}))^2 \rangle - \langle (L_{median}(\tilde{\nu}) - L_{model}(\tilde{\nu}))^2 \rangle$. The image shows that above the stack exit $R_{mean} - R_{med}$ is near zero, on the order of $10^{-4} \mu\text{W}/\text{cm}^2/\text{sr}/\text{cm}^{-1}$, and for many pixels is negative. The difference is greater further

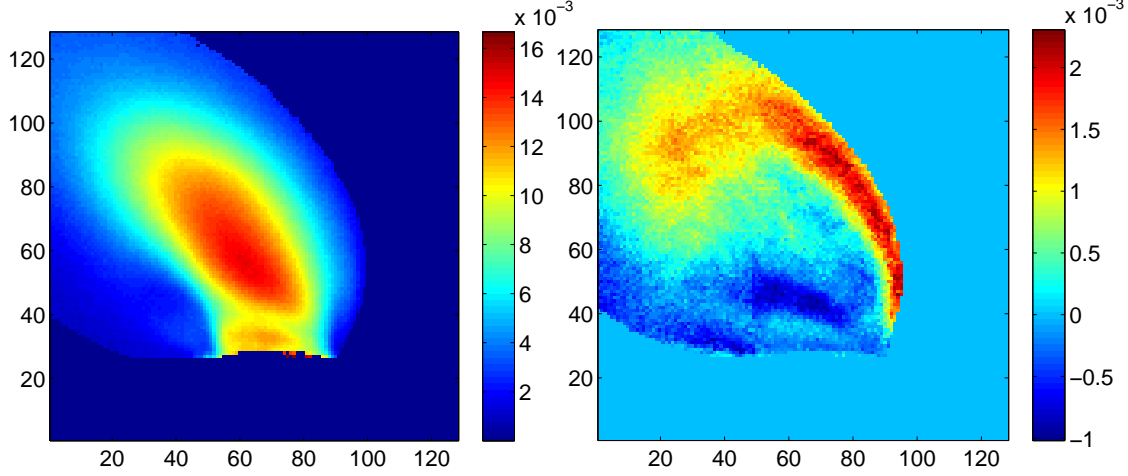


Figure 9. Left: Root mean squared error of $L_{mean}(\tilde{\nu})$ and spectral model (R_{mean}) [$\mu\text{W}/\text{cm}^2/\text{sr}/\text{cm}^{-1}$]. Right: $R_{mean} - R_{med}$ [$\mu\text{W}/\text{cm}^2/\text{sr}/\text{cm}^{-1}$].

up the plume and along the more turbulent right edge of the plume (also visible in the difference between the $L_{mean}(\tilde{\nu})$ and $L_{med}(\tilde{\nu})$ in Figure 7). The low difference between R_{mean} and R_{med} above the stack exit demonstrates that the mean is an appropriate means of estimating effluent concentrations in this region. The effluent concentrations can be precisely determined only in the region directly above the stack exit where the pathlength is known to be equal to the stack diameter. The concentrations cannot be determined exactly farther up in the plume because the exact pathlength is unknown. Thus because any bias introduced by using the mean spectra is negligible in the area of interest, simply time-averaging the spectra is sufficient for accurate effluent concentration estimates. The areas of greater difference in R_{mean} and R_{med} demonstrate areas where turbulence could be a potential problem in determining temperature and effluent concentrations.

The similarity between the fits of the mean and median spectra is also apparent in Figure 10. The top row of Figure 10 shows the mean brightness temperature (T_B^{mean}), the difference between T_B^{mean} and T_B^{med} (median brightness temperature), the standard deviation of T_B ($s_{T_B}^+$), and the difference between two s_{T_B} estimates ($s_{T_B}^+ - s_{T_B}^-$). $s_{T_B}^+$

was estimated from $Q_{+1s} - Q_{med}$, and $s_{T_B}^-$ was estimated from $Q_{med} - Q_{-1s}$. Figure 10 also shows the fit results of the mean spectra for all the three fit parameters, as well as the difference between the mean and median fit results, the standard deviation of the fit results, and the difference between two standard deviation estimates. The mean temperature (T_{mean}) image highlights the areas of highest T_{mean} to be above the stack exit, with T_{mean} diminishing the farther up the plume. T_{mean} directly above the stack exit is on average 395 K (as is T_{med}), which compares favorably to the *in situ* temperature of 394 K. The mean CO₂ column density ($q_{CO_2}^{mean}$) map shows the areas of greatest $q_{CO_2}^{mean}$, approximately 43 cm, in the center of the plume, with lower $q_{CO_2}^{mean}$ closer to the edges of the plume. Directly above the stack exit $q_{CO_2}^{mean}$ is on average 25 cm or 6% (as is $q_{CO_2}^{med}$), compared to an *in situ* measurement of 8.5%. The mean soot transmittance (τ_p^{mean}) image (bottom left panel) shows a similar pattern of lower τ_p^{mean} in the center of the plume, and greater τ_p^{mean} along the edges. Above the stack exit, τ_p^{mean} is approximately 0.97.

The differences between T_{mean} and T_{med} are low (within about ± 1 K) above the stack exit. The area on the right hand edge of the plume where the T_{mean} is much less than that of the T_{med} corresponds to the area of the plume where the difference between R_{mean} and R_{med} is the greatest (Figure 9). The differences between $q_{CO_2}^{mean}$ and $q_{CO_2}^{med}$ are near zero across most to the stack exit (less than 1 cm) and are much greater towards the right hand edge and top half of the plume. The map of the difference between τ_p^{mean} and τ_p^{med} shows a similar pattern, with the lowest differences nearer the stack exit (on the order of -10^{-3} or less) and the greatest differences in the top half and right hand edge of the plume. The similarity between the mean and median fit results for the three parameters near the stack exit further demonstrates that there is little bias in using the time-averaged spectra. The similarity in T_B^{mean} and T_B^{med} above the stack exit indicates this to be a fairly steady region. The simi-

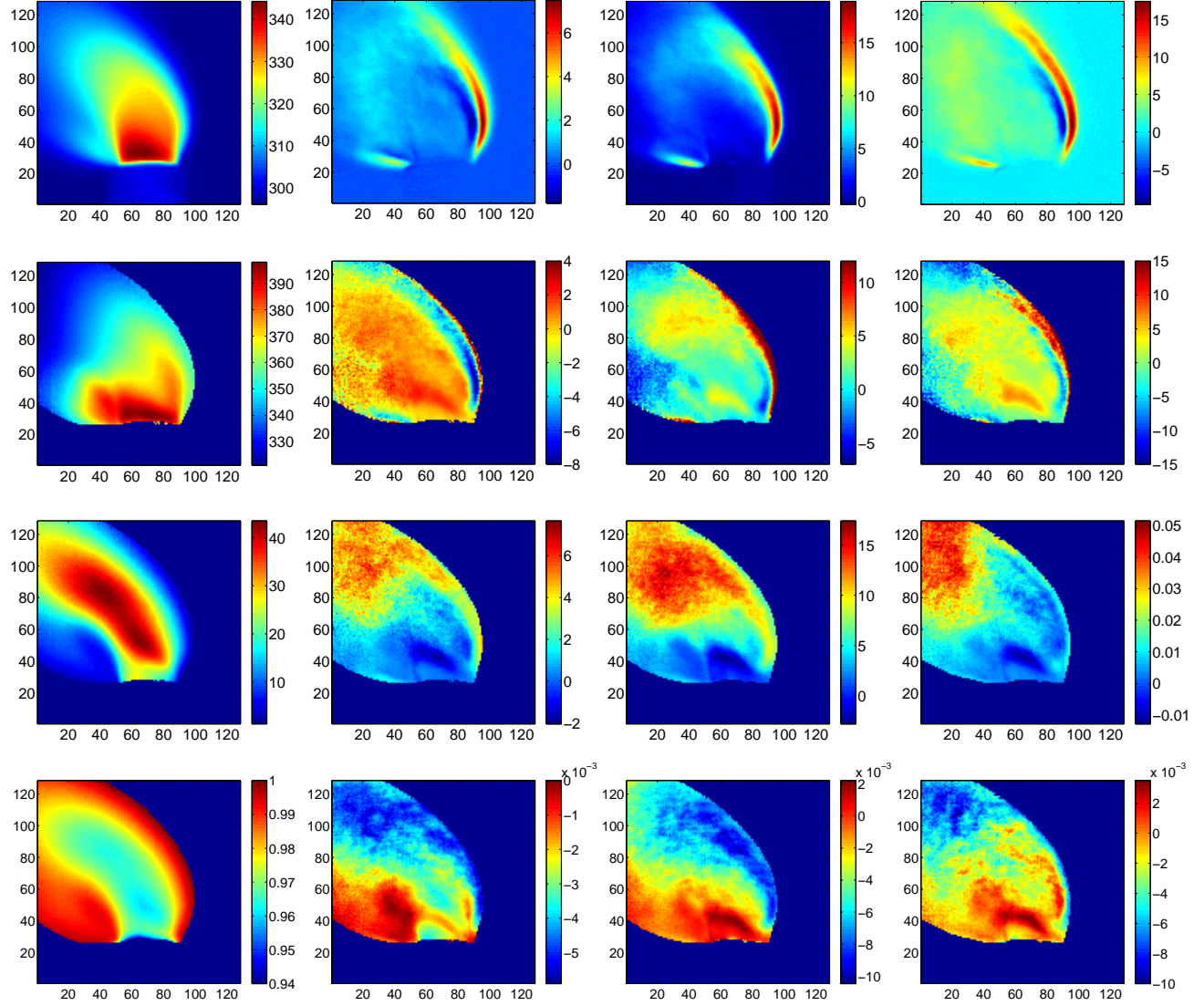


Figure 10. Top row (from left to right): T_B^{mean} , $T_B^{mean} - T_B^{med}$, s_{T_B} , and the difference in two s_{T_B} estimates. Second row (from left to right): T_{mean} (K), $T_{mean} - T_{med}$ (K), s_T (K), and the difference in two s_T estimates. Third row (from left to right): $q_{CO_2}^{mean}$ (cm), $q_{CO_2}^{mean} - q_{CO_2}^{med}$ (cm), s_q (cm), and the difference in two s_q estimates (cm). Bottom row (from left to right): Mean τ_p , $\tau_p^{mean} - \tau_p^{med}$, s_τ , the difference in two s_τ estimates. Standard deviations were estimated from the $Q_{+1s} - Q_{med}$. Difference in standard deviation estimated from $(Q_{+1s} - Q_{med}) - (Q_{med} - Q_{-1s})$.

larity of the fit results in this region proves that this region is in fact steady enough that temperature fluctuations do not introduce systematic errors larger than those already present due to use of a simple, single temperature model.

The standard deviation maps in Figure 10, approximated from $Q_{+1s} - Q_{med}$, are an estimate of how much each parameter is changing. The standard deviation of T (s_T^+) is greatest along the outer right hand edge of the plume (corresponding to the same region of high standard deviation of the T_B) and low above the stack exit (within about 2 K). The standard deviation of q_{CO_2} (s_q^+) is lowest near the stack exit (within about 1 cm) and greater farther up the plume and along the right hand edge of the plume, a pattern also demonstrated by the difference in $q_{CO_2}^{mean}$ and $q_{CO_2}^{med}$. The standard deviation of τ_p (s_τ^+) shows a very similar pattern and is also lowest along the stack exit (within about 10^4) and greater farther up the plume and along the right hand side. The large standard deviations in the right hand edge are likely an effect of wind, causing the plume to move in and out of the field of view of the pixels in that region. As would be expected, the plume's changing density and pathlength farther from the stack exit contribute to more changes in radiance and thus larger s_T , s_q , and s_τ . The right hand column in Figure 10 represents the difference in two standard deviation estimates (Δs) of the T_B , T , q_{CO_2} , and τ_p . Δs is calculated from $(Q_{+1s} - Q_{med}) - (Q_{med} - Q_{-1s})$. Assuming only one parameter is fluctuating, Δs represents the degree of symmetry of the underlying probability density function of that parameter. These images show the areas of the plume where the probability density function deviates the most from a symmetric distribution. For example, the T_B image shows Δs to be greatest along the outer right hand edge of the plume, and low near the stack exit. Δs of the kinetic temperature is also greatest along the outer right hand edge (indicating a region where the temperature distribution is least symmetric) and low near the stack exit. Δs of the column density is greatest in the top half of the plume (indicating a region where the column density distribution is least symmetric) and low near the stack exit. Δs of the τ_p is also low at the stack exit and greatest toward the top of plume. The low Δs for all three parameters above the stack exit

indicates this to be a region of high symmetry.

The standard deviation images in Figure 10 demonstrate that temperature is not the only parameter fluctuating. The assumption that temperature is the only parameter fluctuating allowed quantile spectra to be mapped to a single temperature. The difference between CO₂ column densities and soot transmittances retrieved from quantile spectra should therefore be zero, which is not the case in Figure 10. While the method of sorting the spectra into quantiles is still valid, the monotonic relationship between I_{DC} and temperature falls apart and these quantile spectra can no longer be mapped to a specific temperature. Rather, each quantile spectrum maps to a collection of temperature and concentration pairs that all correspond to the same integrated radiance, and quantitative conclusions cannot be drawn. Thus because temperature is not the only parameter varying, the underlying temperature distribution cannot be inferred and accurate estimates of temperature fluctuations obtained. However, sorting the data into quantiles before fitting to the model still provides information that simply time-averaging the spectra does not. Although fitting a quantile spectrum to the model gives only one of the temperature and concentration pairs possible, it still provides a sample of the underlying temperature and concentration distribution not provided by the time-averaged spectrum. Quantile spectra can still reveal a good deal of spatial information, as demonstrated by the standard deviation and Δs maps in Figure 10. Figure 10 shows clear spatial patterns in the standard deviation and Δs images. Considering the fact that each pixel was treated independently, these patterns are representative of real phenomena in the plume. For flow fields in which multiple parameters are randomly fluctuating, retrieval of the underlying joint probability density function from the mean spectrum is difficult if not impossible without considerable *a priori* knowledge of its general form. Quantile spectra, however, can provide additional constraining data for this retrieval process and may improve the

success of such a method.

Figure 11 shows the fit results of several pixels for the three parameters along with the 95% confidence intervals for Q_{med} , $Q_{\pm 0.5s}$, and $Q_{\pm 1s}$. The median value has been subtracted from each curve. Although trends can be seen in the figures, the confidence intervals overlap significantly, making it difficult to draw any quantitative statistical information from the results. Trends, however, can be still observed in the results. No real trend in T or q_{CO_2} is apparent in the pixel directly above the stack exit (35, 65). In the pixel in the center of the plume (62, 61), T appears flat with increasing probability, however q_{CO_2} appears to increase. Any trend in temperature is difficult to discern at pixel (118, 16) since the T appears flat with the exception of

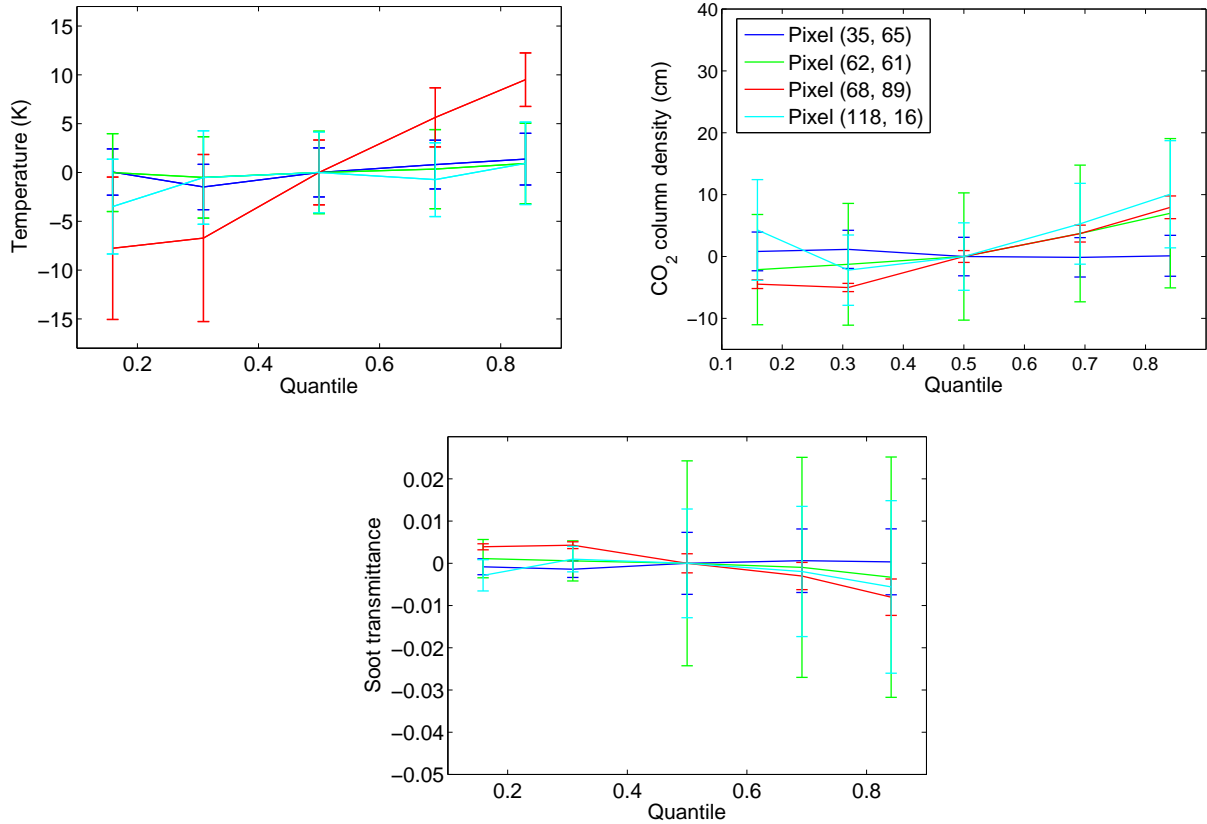


Figure 11. From left to right: T (K), q_{CO_2} , and τ_p of several pixels for Q_{med} , $Q_{\pm 0.5s}$, and $Q_{\pm 1s}$ with 95% confidence intervals. The median has been subtracted from each curve.

the tails of the curve. A trend in q_{CO_2} at pixel (118, 16) is also difficult to discern because q_{CO_2} falls and rises in the center of the curve. τ_p appears fairly flat with the exception of the tails of the curves for every pixel except (68, 89), where it does exhibit a downward trend. Pixel (68, 89) also demonstrates a trend of both increasing T and q_{CO_2} with probability. Even considering overlapping confidence intervals, all three parameters for pixel (68, 89) exhibited change as probability increased in this turbulent region of the plume.

3.5.3 Turbulence Simulations.

Although the similarity of the fit results above the stack exit demonstrated that temperature and concentration fluctuations were small enough for use of a single temperature model to accurately determine concentrations, at some point the fluctuations become too large and the model breaks down. Simulations were performed to investigate the error introduced by the use of a single temperature model to interpret the mean spectrum of a turbulent source. The average radiance of the source with only the temperature fluctuating can be represented by Equation 18. $P(T)$ was chosen to be a Gaussian distribution with a mean 396 K, and the standard deviation (s_T) was varied from 0 to 20 K. The average radiance, $L_{mean}(\tilde{\nu})$, was compared to the radiance at the average temperature, $L(T_{mean})$, for each $P(T)$. The same simulation was performed for a source with only a fluctuating CO₂ concentration. In this case, $P(T)$ in Equation 18 is replaced with a probability distribution of CO₂ concentration. A Gaussian distribution with a mean of 25.4 cm (6%) and a standard deviation (s_q) that ranged from 0 to 15.3 cm (3.6%) were chosen. The top left plot in Figure 12 represents the error (R) as function of s_T for the case of $s_q = 0$ (concentration not fluctuating), where $R = \langle (L_{mean}(\tilde{\nu}) - L(T_{mean}))^2 \rangle$. The top right plot represents the error (R) as a function of s_q for the case of $s_T = 0$ (temperature not fluctuating),

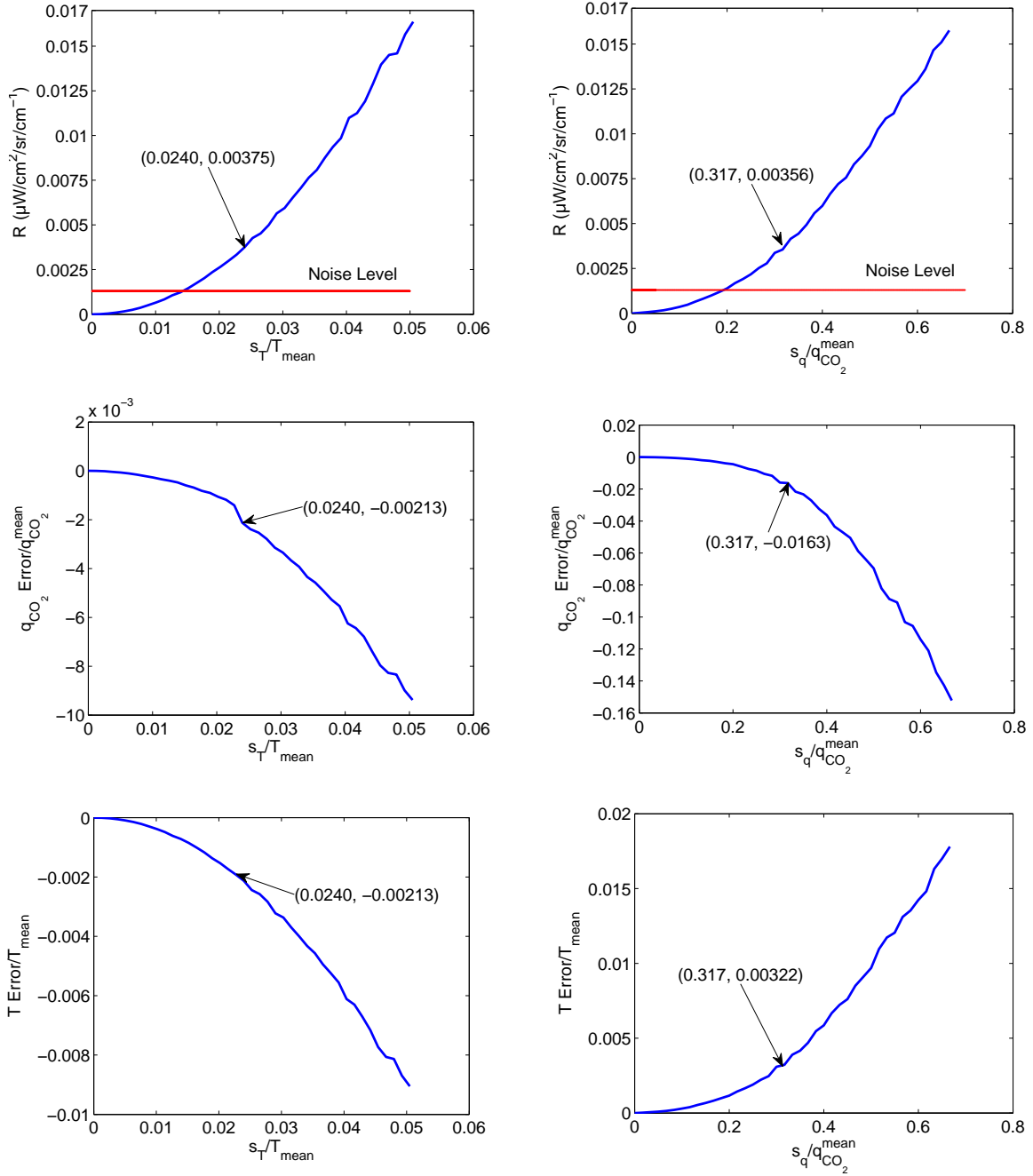


Figure 12. Top row: Root mean square of $L_{mean}(\tilde{\nu}) - L(T_{mean}, q_{CO_2}^{mean})$ (R) [$\mu W/cm^2/sr/cm^{-1}$] as a function of s_T/T_{mean} (left) and as a function of $s_q/q_{CO_2}^{mean}$ (right). Center row: q_{CO_2} error ($q_{CO_2}^{mean} - q_{CO_2}$ corresponding to $L_{mean}(\tilde{\nu})$) as a function of s_T/T_{mean} (left) and as a function of $s_q/q_{CO_2}^{mean}$ (right). Bottom row: T error ($T_{mean} - T$ corresponding to $L_{mean}(\tilde{\nu})$) as a function of s_T/T_{mean} (left) and as a function of $s_q/q_{CO_2}^{mean}$ (right). $T_{mean} = 396$ K, and is representative of T_{mean} above the stack exit. $q_{CO_2}^{mean} = 25$ cm (6%), and is representative of $q_{CO_2}^{mean}$ above the stack exit. Only one parameter was varied at a time.

where $R = \langle (L_{mean}(\tilde{\nu}) - L(q_{CO_2}^{mean}))^2 \rangle [\mu\text{W}/\text{cm}^2/\text{sr}/\text{cm}^{-1}]$. s_T and s_q are presented as fractions of the T_{mean} and $q_{CO_2}^{mean}$ at the stack exit. The center plots in Figure 12 represent the error in temperature normalized by T_{mean} as a function of the relative T fluctuations (left) and relative q_{CO_2} fluctuations (right). The temperature error corresponds to $T_{mean} - T$ determined from the mean spectrum. The bottom plots in Figure 12 represent the error in q_{CO_2} normalized by $q_{CO_2}^{mean}$ as a function of relative T fluctuations (left) and relative q_{CO_2} fluctuations (right). q_{CO_2} error corresponds to $q_{CO_2}^{mean} - q_{CO_2}$ determined from the mean spectrum.

Because only 1000 temperatures and concentrations were sampled, plotting the error as a function of the relative temperature and concentration fluctuations resulted in somewhat jagged curves. In order to smooth out the results, the above analysis was performed several times for each case ($s_T = 0$ and $s_q = 0$) and averaged. According to Figure 12, a 1.9% CO_2 concentration fluctuation (32% of $q_{CO_2}^{mean}$) is required to give the same overall error ($0.0038 \mu\text{W}/\text{cm}^2/\text{sr}/\text{cm}^{-1}$ or 3 times the noise level of the instrument) as a 9.5 K temperature fluctuation (2.4% of T_{mean}). This same pattern is observed in the T error and q_{CO_2} error plots. If only one parameter is fluctuating, a much larger q_{CO_2} fluctuation than T fluctuation is needed obtain the same errors in T and q_{CO_2} . Thus if only one parameter is fluctuating, temperature fluctuations have a much greater impact on the quality of the fit results than concentration fluctuations.

The relative importance of the error in T and q_{CO_2} can be examined by comparing the relative errors at the s_T and s_q that result in the same overall error in the spectrum. Table 1 contains the relative T and q_{CO_2} errors corresponding to an overall error, R , of $0.0038 \mu\text{W}/\text{cm}^2/\text{sr}/\text{cm}^{-1}$ for each case. The arrows in Figure 12 indicate the value of s_T and s_q that result in an overall error, R , of $0.0038 \mu\text{W}/\text{cm}^2/\text{sr}/\text{cm}^{-1}$. A comparison of the relative T and q_{CO_2} errors at these values reveals that if only T fluctuates, the relative errors are the same. If only q_{CO_2} is fluctuating, the magnitude

of the relative q_{CO_2} error is approximately 5 times greater than that of the relative T error, indicating that in this case q_{CO_2} error has a greater influence on the overall error in the spectrum.

Table 1. Temperature and CO₂ concentration errors corresponding to an overall error, R , equal to $0.0038 \mu\text{W}/\text{cm}^2/\text{sr}/\text{cm}^{-1}$ for each case ($s_T = 0$ and $s_q = 0$).

		Temperature Fluctuating: $s_T = 0.024$ (9.5 K)	Concentration Fluctuating: $s_q = 0.32$ (0.019% or 8.1 cm)
R:		$0.0038 \mu\text{W}/\text{cm}^2/\text{sr}/\text{cm}^{-1}$	$0.0039 \mu\text{W}/\text{cm}^2/\text{sr}/\text{cm}^{-1}$
T Error/ T_{mean} :		-0.21% (-0.84 K)	0.36% (1.4 K)
q_{CO_2} Error/ q_{CO_2} mean:		-0.21% (0.013% or 0.054 cm)	-1.9% (-0.11% or -0.47 cm)

The method used to obtain the standard deviation images in Figure 10 is based on the assumption that only the temperature of the source is fluctuating. Although the s_q map clearly shows that q_{CO_2} is fluctuating, the corresponding T and q_{CO_2} errors can still be found under the assumption that only one parameter is fluctuating. For example, the pixels in the s_T image can be connected with the T and q_{CO_2} errors that would result if only the temperature was fluctuating. Table 2 contains the T and q_{CO_2} errors corresponding to the s_T and s_q of pixels (35, 65) and (68, 89). Pixel (35, 65) is in the region above the stack exit, and pixel (68, 89) is in the turbulent right hand edge of the plume. The results in Table 2 demonstrate that if only temperature or concentration fluctuates, the standard deviations found in the turbulent region of the plume result in substantial errors due to use of a single temperature model.

Table 2. Temperature and CO₂ concentration errors corresponding to the s_T and s_q of pixels (35, 65) and (68, 89).

		Temperature Fluctuating		Concentration Fluctuating	
		Pixel (35, 65): $s_T = 1.4$ K	Pixel (68, 89): $s_T = 9.5$ K	Pixel (35, 65): $s_q = 0.11$ cm	Pixel (68, 89): $s_q = 8.0$ cm
T Error:		0.02 K	-0.84 K	0.003 K	1.3K
q_{CO_2} Error:		$-4 \times 10^{-4}\%$ (-9×10^{-4} cm)	-0.013 % (-0.054 cm)	-1×10^{-4} % (-5×10^{-4} cm)	-0.098 % (-0.41 cm)

3.6 Conclusions and Recommendations

The similarity in the mean and median fit results immediately above the smokestack exit serves to increase the confidence in temperature and effluent concentrations obtained by IFTS. Because effluent concentrations are readily derived from column densities above the stack exit where the plume geometry is known, the similarity in the mean and median fit results in this region demonstrates that the mean spectrum is sufficient for determining effluent concentrations. The similarity in the mean and median fit results above the stack exit demonstrates that this region is steady enough for use of the mean spectrum to estimate temperature and effluent concentrations. The ability of IFTS to isolate the area above the stack exit makes it an ideal method for determining effluent concentrations of smokestack plumes. While IFTS has the capability of identifying the turbulent and steady regions of the plume, non-imaging FTS does not.

While this research demonstrated the similarity of the mean and median spectra directly above the stack exit, the mean and median spectra differed significantly in regions affected by turbulence in the plume or other causes (such as wind) of temporal radiance variations. Nonetheless, approximate temperature and CO₂ column densities were retrieved throughout the plume. Even though fit residuals were small, the spatial pattern in the root mean square fit error demonstrates the imperfections in the spectral model. This spatial pattern may indicate the presence of information in the spectra about temperature and concentration gradients along the line of sight that could potentially be recovered from the spectrum.

IFTS also presents an advantage in its ability to provide additional information not provided by non-imaging FTS. Imaging spectrometers retain the DC component of intensity, allowing the statistical sorting of the spectra, a capability not provided by non-imaging spectrometers. While the results of this research showed that each

quantile spectrum could not be mapped to a specific temperature and therefore the underlying temperature distribution could not be inferred, standard deviation and Δs maps obtained by the statistical sorting of the spectra provided considerable spatial information not contained in the mean spectrum. These maps demonstrate the amount of information contained in the quantile spectra as well as the potential of quantile spectra for flow field diagnostics. Quantile spectra contain considerable additional information, and the interpretation of quantile spectra and their application to flow field diagnostics is worth further investigation.

Appendix A. Matlab Code

The code in this appendix sorts the raw interferograms into quantiles and creates quantile interferograms for data cubes in only one direction. Only the median, $\pm 1s$, and $\pm 2s$ quantile interferograms are shown, however, any number of quantile interferograms can be created.

Listing A.1.

```
1 %% Creates quantile interferogram matrices for data cubes in 1 ...
    direction

% Inputs:
xsize=128; %size of window in x-direction
ysize=128; %size of window in y-direction
6 sw=948; %sampling window dimension
sweepdir = 1; %sweep direction: forward = 1, reverse = 0
files = dir('DAT*F_OC.raw'); %file prefix for data cubes of ...
    interest

%Create empty matrices the size:
11 %(# of data rows)x(# columns)x(sampling window dimension)
    q_median = zeros(ysize,xsize,sw); % Median quantile
    q_p1s = zeros(ysize,xsize,sw); %+1s quantile
    q_p2s = zeros(ysize,xsize,sw); %+2s quantile
    q_m1s = zeros(ysize,xsize,sw); %-1s quantile
16 q_m2s = zeros(ysize,xsize,sw); %-2s quantile

nFiles = length(files); %Number of cubes
Data = zeros(nFiles, xsize, sw); %Create an empty matrix the size:
    %(# data cubes in chosen direction)x(# columns)x(sampling window ...
        dimension)
21
```

```

%Imports and finds the various quantiles one row at a time for all...
    data cubes in the specified direction.
progressbar(0);
for jj = 1:ysize %jj is row number
    k=1;
26 for ii = 1:nFiles
        fname = files(ii).name;
        [~,~,hd]=importTelops(fname,'header'); %Imports just the ...
            header information for each datacube.
            if hd.DCA_SweepDirection==sweepdir %Imports only the data ...
                cubes in the specified direction.
                [Data(k,:,:),~,H] = importTelops(fname,'row',jj,1); %3...
                    x3 Matrix of all datacubes in specified direction.
31         k=k+1;
            end
        end
    end
    for n=1:sw %Finds each quantile from the matrix of data cubes
        q_median(jj,:,n) = quantile(Data(:,:,n),0.5,1);
36        q_p1s(jj,:,n) = quantile(Data(:,:,n),0.841,1);
            q_p2s(jj,:,n) = quantile(Data(:,:,n),0.977,1);
            q_m1s(jj,:,n) = quantile(Data(:,:,n),0.159,1);
            q_m2s(jj,:,n) = quantile(Data(:,:,n),0.023,1);
        end
41 progressbar(jj/ysize);
    end

%Reshape matrices for calibration to radiance units:
rq_median=reshape(permute(q_median,[2 1 3]),xsize*ysize,sw);
46 rq_p1s=reshape(permute(q_p1s,[2 1 3]),xsize*ysize,sw);
    rq_p2s=reshape(permute(q_p2s,[2 1 3]),xsize*ysize,sw);
    rq_m1s=reshape(permute(q_m1s,[2 1 3]),xsize*ysize,sw);
    rq_m2s=reshape(permute(q_m2s,[2 1 3]),xsize*ysize,sw);

```

Bibliography

- [1] HW Prengle, CA Morgan, CS Fang, LK Huang, P Campani, and WW Wu. Infrared Remote Sensing and Determination of Pollutants in Gas Plumes. *Environmental Science & Technology*, 7(5):417–423, 1973.
- [2] Rainer Haus, Klaus Schaefer, Joanna I. Hughes, Joerg Heland, and Wilfried Bautzer. Ftis remote sensing of smokestack and test flare emissions. volume 2506, pages 45 – 54, /unich, Ger, 1995. Flare emissions;Smokestack plumes;.
- [3] K. Schafer, J. Heland, D.H. Lister, C.W. Wilson, R.J. Howes, R.S. Falk, E. Lindermeir, M. Birk, G. Wagner, P. Haschberger, M. Bernard, O. Legras, P. Wiesen, R. Kurtenbach, K.J. Brockmann, V. Kriesche, M. Hilton, G. Bishop, R. Clarke, J. Workman, M. Caola, R. Geatches, R. Burrows, J.D. Black, P. Herve, and J. Vally. Nonintrusive optical measurements of aircraft engine exhaust emissions and comparison with standard intrusive techniques. *Applied Optics*, 39(3):441 – 455, 2000.
- [4] W.F. Herget. Remote and cross-stack measurement of stack gas concentrations using a mobile ft-ir system. *Applied Optics*, 21(4):635 – 641, 1982.
- [5] M. Hilton, A.H. Lettington, and I.M. Mills. Quantitative analysis of remote gas temperatures and concentrations from their infrared emission spectra. In *Measurement Science & Technology*, volume 6, pages 1236 – 1241, J.J. Thomson Phys. Lab., Reading Univ., UK, 1995.
- [6] RC Carlson, AF Hayden, and WB Telfair. Remote observations of effluents from small building smokestacks using ftir spectrosc. *Applied Optics*, 27(23):4952–4959, DEC 1 1988.
- [7] Kevin C. Gross, Kenneth C. Bradley, and Glen P. Perram. Remote identification and quantification of industrial smokestack effluents via imaging fourier-transform spectroscopy. *Environmental Science & Technology*, 2010.
- [8] K.C. Bradley, S. Bowen, K.C. Gross, M.A. Marciniak, and G.P. Perram. Imaging fourier transform spectrometry of jet engine exhaust with the telops first-mwe. In *Aerospace conference, 2009 IEEE*, pages 1 –8, 7-14 2009.
- [9] Elizabeth A. Moore, Kevin C. Gross, Spencer J. Bowen, Glen P. Perram, Martin Chamberland, Vincent Farley, Jean-Philippe Gagnon, Philippe Lagueux, and Andre Villemaire. Characterizing and overcoming spectral artifacts in imaging fouriertransform spectroscopy of turbulent exhaust plumes. volume 7304, pages The International Society for Optical Engineering (SPIE) –, Orlando, FL, United states, 2009. FTS;Imaging spectroscopy;Jet engine exhaust;Scene-change artifacts;Source noise;.

- [10] Pierre Tremblay, Kevin C. Gross, Vincent Farley, Martin Chamberland, Andre Villemaire, and Glen P. Perram. Understanding and overcoming scene-change artifacts in imaging fourier-transform spectroscopy of turbulent jet engine exhaust. volume 7457, pages The International Society for Optical Engineering (SPIE) –, San Diego, CA, United states, 2009. Hyperspectral;Imaging Fourier-transform spectrometer (IFTS);Interferogram;Median;Quantile;Scene-change artifacts;.
- [11] L.S. Rothman, D. Jacquemart, A. Barbe, D. Chris Benner, M. Birk, L.R. Brown, M.R. Carleer, C. Chackerian, K. Chance, L.H. Coudert, V. Dana, V.M. Devi, J.-M. Flaud, R.R. Gamache, A. Goldman, J.-M. Hartmann, K.W. Jucks, A.G. Maki, J.-Y. Mandin, and S.T. Massie. The hitran 2004 molecular spectroscopic database. *Journal of Quantitative Spectroscopy & Radiative Transfer*, 96(2):139 – 204, 2005.
- [12] Sumner P. Davis, Mark C. Abrams, and James W. Brault. *Fourier Transform Spectrometry*. Academic Press, 2001.
- [13] Gary E. Thomas and Knut Stamnes. *Radiative Transfer in the Atmosphere and Ocean*. Cambridge University Press, 1999.
- [14] S.A. Clough, M.W. Shephard, E.J. Mlawer, J.S. Delamere, M.J. Iacono, K. Cady-Pereira, S. Boukabara, and P.D. Brown. Atmospheric radiative transfer modeling: a summary of the aer codes. *Journal of Quantitative Spectroscopy & Radiative Transfer*, 91(2):233 – 244, 2005.
- [15] Joseph H.W. Lee and Vincent H. Chu. *Turbulent Jets and Plumes: A Lagrangian Approach*. Kluwer Academic Publishers, 2003.
- [16] Panos N. Papanicolaou and E. John List. Investigations of round vertical turbulent buoyant jets. *Journal of Fluid Mechanics*, 195:341–391, 1988.

REPORT DOCUMENTATION PAGE					Form Approved OMB No. 0704-0188	
<p>The public reporting burden for this collection of information is estimated to average 1 hour per response, including the time for reviewing instructions, searching existing data sources, gathering and maintaining the data needed, and completing and reviewing the collection of information. Send comments regarding this burden estimate or any other aspect of this collection of information, including suggestions for reducing this burden to Department of Defense, Washington Headquarters Services, Directorate for Information Operations and Reports (0704-0188), 1215 Jefferson Davis Highway, Suite 1204, Arlington, VA 22202-4302. Respondents should be aware that notwithstanding any other provision of law, no person shall be subject to any penalty for failing to comply with a collection of information if it does not display a currently valid OMB control number. PLEASE DO NOT RETURN YOUR FORM TO THE ABOVE ADDRESS.</p>						
1. REPORT DATE (DD-MM-YYYY)		2. REPORT TYPE		3. DATES COVERED (From — To)		
24-03-2011		Master's Thesis		Aug 2009 — Mar 2011		
4. TITLE AND SUBTITLE Understanding the Influence of Turbulence in Imaging Fourier-Transform Spectrometry of Smokestack Plumes				5a. CONTRACT NUMBER		
				5b. GRANT NUMBER		
				5c. PROGRAM ELEMENT NUMBER		
6. AUTHOR(S) Massman, Jennifer L., 2d Lt, USAF				5d. PROJECT NUMBER		
				5e. TASK NUMBER		
				5f. WORK UNIT NUMBER		
7. PERFORMING ORGANIZATION NAME(S) AND ADDRESS(ES) Air Force Institute of Technology Graduate School of Engineering and Management (AFIT/EN) 2950 Hobson Way WPAFB OH 45433-7765				8. PERFORMING ORGANIZATION REPORT NUMBER AFIT/GAP/ENP/11-M05		
9. SPONSORING / MONITORING AGENCY NAME(S) AND ADDRESS(ES) Intentionally Left Blank				10. SPONSOR/MONITOR'S ACRONYM(S)		
				11. SPONSOR/MONITOR'S REPORT NUMBER(S)		
12. DISTRIBUTION / AVAILABILITY STATEMENT APPROVED FOR PUBLIC RELEASE; DISTRIBUTION UNLIMITED.						
13. SUPPLEMENTARY NOTES						
14. ABSTRACT <p>An imaging Fourier-transform spectrometer (IFTS) was used to collect infrared hyper-spectral imagery of smokestack plume of a coal-burning power facility to assess the influence of turbulence on spectral retrieval of temperature (T) and pollutant concentrations (C_i). Radiance fluctuations due to plume turbulence introduced scene change artifacts (SCA) in the spectra. Time-averaging the spectra minimizes SCA magnitudes, but accurate T and C_i retrieval would require a priori knowledge of the statistical distribution of temperature and other stochastic flow field parameters. A method of quantile sorting in interferogram space that would allow the retrieval of the temperature distribution is presented and used to identify turbulence throughout the plume. Immediately above the stack exit, T and C_i estimates compared well to <i>in situ</i> measurements, and turbulence introduced only small systematic errors. Systematic errors, however, were more significant in other parts of the plume. While more complicated radiance fluctuations precluded retrieval of the temperature distribution, the results demonstrate the utility of additional information associated with interferogram quantiles and suggest the utility of IFTS in non-intrusive flow field analysis.</p>						
15. SUBJECT TERMS hyper-spectral imaging, imaging Fourier transform spectrometry, smokestack plume, turbulence, temperature distribution						
16. SECURITY CLASSIFICATION OF:			17. LIMITATION OF ABSTRACT	18. NUMBER OF PAGES	19a. NAME OF RESPONSIBLE PERSON	
a. REPORT	b. ABSTRACT	c. THIS PAGE			Dr. Kevin C. Gross	
U	U	U	U	63	19b. TELEPHONE NUMBER (include area code) (937) 255-3636, x4558; kevin.gross@afit.edu	